IMPERIAL COLLEGE LONDON

Department of Mechanical Engineering

MINIMALLY INVASIVE TREATMENT OF LONG-BONE FRACTURES: A FINITE ELEMENT ANALYSIS

Jack Chester

FINAL REPORT

ME4 Individual Project

Supervised by *Dr Richard van Arkel*

03 MAY 2021

Word Count: 11,925 / 12,000

[Excluding Figures]

ABSTRACT

Chronic, painful and debilitating complications are common in the treatment of long-bone fractures. 23% of cases, for example, culminate in the worst possible clinical outcome of non-union. These issues arise due to constructs being biomechanically incompatible with the patient-specific environments they are implanted within. Therefore, in the context of simple, tibial, mid-shaft fractures, fixated by means of a statically locked and reamed intramedullary nail (IMN), this project strived to present findings that surgeons can use to better inform their construct configuration decisions, thus improving treatment prognoses.

To accomplish this, a novel and innovative Finite Element framework has been developed that sees the screw-bone interface modelled using a tuned set of springs, together with tuned frictional softened contacts, to grant an accurate assessment of the healing potential of IMN fixated fractures, for the very first time. An extensive set of sensitivity studies subsequently validated its performance, permitting its use as a tool for accurately quantifying the implications of fracture geometry, primary intervention strategy, degree of weight bearing, and revisionary surgical technique in a single, unambiguous study.

Fractures of greater obliquity, with larger gaps, and of orientation that is tending towards the AP direction have all been found to promote non-union through a marked elevation of shear motion at the fracture site. Different screw configurations have been shown to have little effect as compared to the nail diameter, which can approximately double the stability for every 1 mm incrementation in its size. Furthermore, 50% weightbearing following surgery has been deemed most appropriate. Finally, the insertion of three minimally invasive screws perpendicular to the fracture site has been shown to have the same stabilizing effect as an exchange nail 1mm larger in diameter than that of the original nail. It is hoped that such findings that will profoundly impact clinical proceedings in this field for years to come.

TABLE OF CONTENTS

1 INTRODUCTION

Some portions of this report have been adapted from [1]*, yet for brevity this shall not be repeated through the document.*

On average, an individual can expect to fracture two bones in their lifetime . This translates to an annual fracture admission rate of approximately 250,000 in the UK alone [2] – a number that is likely to escalate over future years due to an anticipated rise in life expectancy and thus a reduction in bone density and toughness of a typical UK civilian.

The toolbox of any orthopaedic surgeon tasked with treating fractures comprises a vast array of constructs and installation techniques [3]. These must be narrowed down to a single configuration that best compliments the bone quality, anatomy, and local loading conditions of the patient [4] if well-aligned consolidation is to be achieved in the shortest possible timeframe [5], whilst minimizing the risk of infection and soft tissue damage, amongst other complications [6]. In the case of long, weight-bearing bones, such as the tibia and femur, which constitute 13% of fracture cases, this denotes a notoriously challenging feat [7]. Hence, complications are common [8], [9].

At present, 23% of long-bone (LB) fractures fail to heal, instead culminating in a chronic, painful, physically disabling and psychologically debilitating health condition that is coined 'non-union' [10]. With the cost of a single surgical revision estimated to be £7,000 - £79,000 [11], much biomechanical research is thus currently being undertaken to inform such treatments, improve their prognoses, and alleviate the significant financial and clinical burden they pose both to the UK and worldwide.

In general, the finite element (FE) method is adopted in preference to conducting in-vivo and in-vitro experiments this field, due to the greater ease with which these types of study can be parameterized. Furthermore, it grants the evaluation of stresses and strains at the bone-implant interfaces, as well as those arising internally within the bone, which would otherwise be troublesome, if not impossible, to measure experimentally. The approach can therefore facilitate a more comprehensive and valuable assessment of the biomechanical performance of various construct types, of differing configuration, subjected to a range of loading conditions, to name just a few variables.

Despite this desirable versatility that the FE method can offer, all of the FE data that has been reported amid the field to date hones solely in on the primary intervention strategy, that is to say how a modification to the parameters of the construct alone, for a given fracture case, may affect healing. No studies address the implications of fracture geometry and degree of weight-bearing, both of which have been shown clinically to bear great significance. Moreover, despite the persistent prevalence of non-unions within society, revisionary surgical techniques are yet to receive any research attention. These sizeable voids are leaving surgeons little choice but to call upon out-dated, unsubstantiated knowledge from training to inform their subjective decisions. Hence, in collaboration with a leading surgeon in the field of orthopaedic trauma at St George's University Hospital, London, this project aims to exploit the FE method to deliver a relevant, self-standing and publishable body of work to which surgeons can resort for a quantitative and unambiguous elucidation of the implications all of their decisions could have on the efficacy of LB fracture treatments.

The following four objectives were defined at the project outset to aid complete fulfilment of this highly ambitious aim:

OBJECTIVE ONE Conduct a literature review of LB fracture primary intervention strategies, revisionary surgical techniques and previous work, to inform the loose specification of an appropriate FE base model (BM) and its parameterization.

OBJECTIVE TWO Exploit state of the art as well as novel FE modelling techniques to develop and set up a functioning BM.

OBJECTIVE THREE Investigate the sensitivity of the BM to various modelling parameters, using the results for the purpose of validation and to inform its conservative enhancement, if required.

OBJECTIVE FOUR Assess the implications of fracture geometry, primary intervention strategy, degree of weight bearing, and revisionary surgical technique on healing performance using the developed modelling framework.

This report seeks to concisely and sequentially delineate the various methodologies and findings associated with each of these objectives, prior to making a statement of future work and explicitly restating the most pertinent project outcomes, which are hoped to have a lasting impact on clinical practise for years to come.

2 BACKGROUND & LITERATURE REVIEW

The succinct review of literature that features in what follows attempts to expand on the intricacy of LB fracture treatments, such that one can begin to appreciate the difficulty of making a given surgical decision, as well as its potential subsequent consequences. Specific voids in the current body of research will also be explicitly highlighted, before outlining a specification for the base model that will directly address these issues. First, some technical terminology pertinent to the comprehension of all work undertaken will first be outlined.

2.1 RELEVANT BIOMECHANICAL TERMINOLOGY

A three tier hierarchal set of biomechanical terminology is typically called upon in the study of LB bone fractures. In the broadest sense, the general *anatomical terms of location* are always used. These comprise three orthogonal planes and a set of six qualitative terms, which together or in solitude may be exploited to highlight the relative position of a region of interest (ROI) with respect to some datum, as depicted in FIGURE 1 opposite.

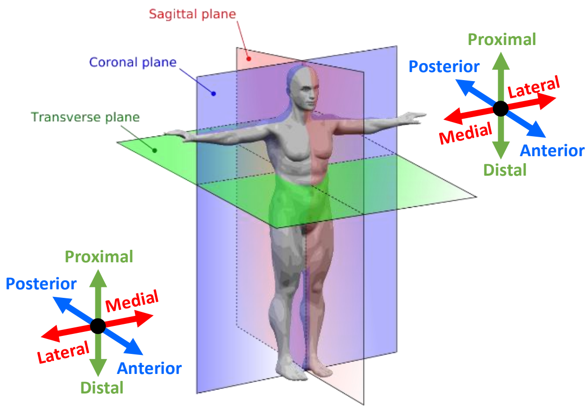

FIGURE 1 | Anatomical terms of location [7] .

Often, on a more refined level, reference must be made to a specific constituent of the *LB anatomy* (see FIGURE 2). The exterior, otherwise known as the *cortex*, is a smooth, dense and exceptionally hard layer of *cortical* bone, beneath which lies a weaker, yet reinforcing, nourishing and sensitive, honeycombed network of spongy, *trabecular* bone. The extensive, straight, central portion of long bone is another important aspect that receives much attention and is termed the shaft, or *diaphysis*. This houses the *marrow* containing *medullary cavity*, and flares out towards either end of the bone's length in regions called *metaphyses*, prior to terminating at the joint surfaces, or *articular* regions, known as *epiphyses*. The *periosteum* and *endosteum* are

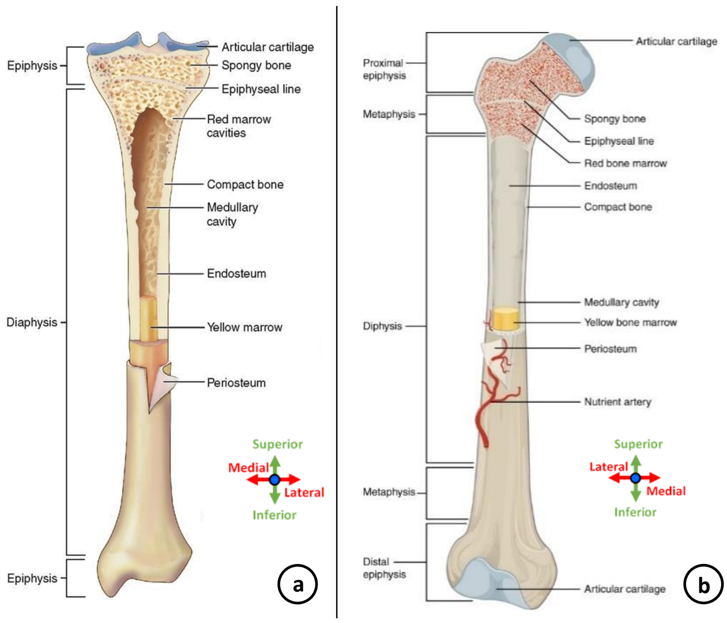

FIGURE 2 | Anatomy of (a) the tibia and (b) the femur [8].

continuous, nourishing internal and external membranes, respectively, that envelope the bone in its entirety [8].

Finally, solely more advanced, bone-specific, specialist terminology will suffice in some instances. Those features that are unique to the shin bone, or *tibia,* and thigh bone, or *femur*, which are touched upon in this report, are annotated in FIGURE 3, below.

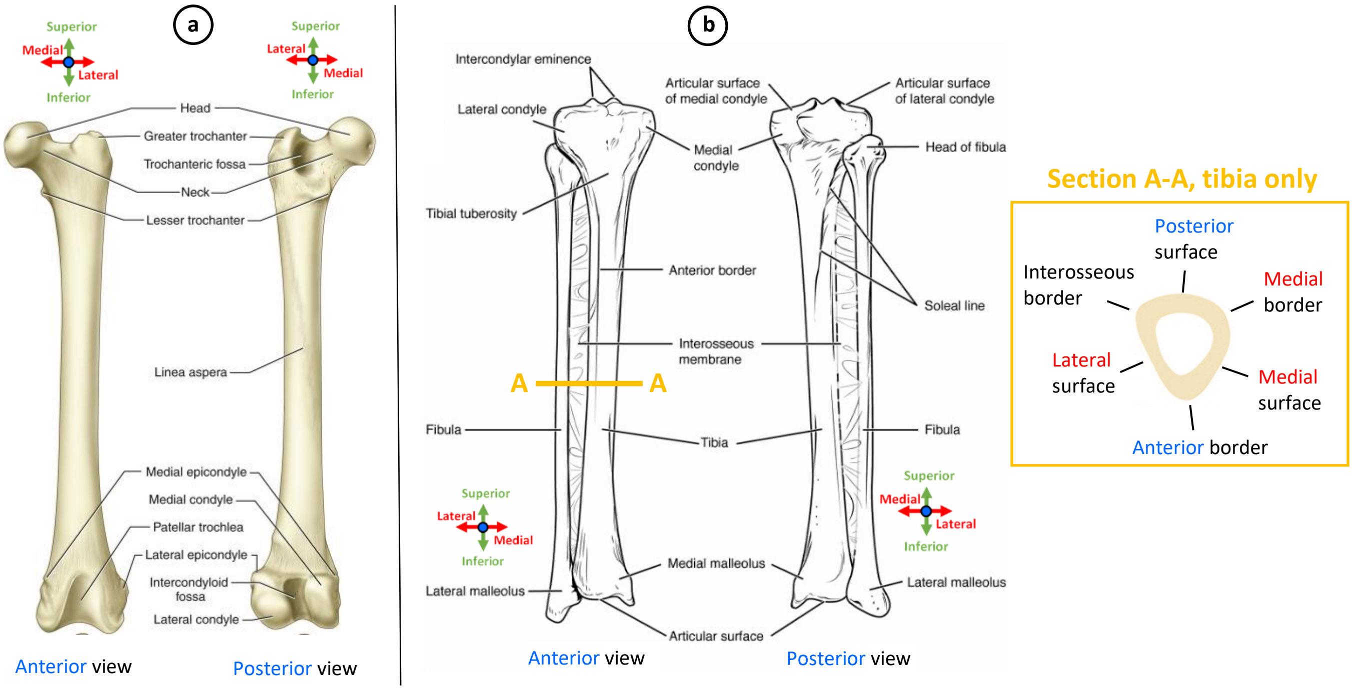

FIGURE 3 | (a) Femur-specific [8] and (b) Tibia-specific terminology that will be used throughout this report [9].

Evidently, one must also be fully acquainted with the different LB fracture types that can be sustained by an adult individual. If the bone does not penetrate the skin, as is often the case, then the fracture may be termed *closed* as opposed to *open*, in the first instance, and subsequently further classified a epiphyseal, metaphyseal or diaphyseal according to its anatomical location along the bone's longitudinal axis [10]. The latter is most common [12], of which there are seven types. These are surmised in TABLE 1 overleaf.

TABLE 1 | The seven types of long bone diaphyseal fractures according to the AO Fracture and Dislocation Classification System [12] substitutes 42 into each of the classification codes when referring to a femoral rather than a tibial fracture and * is replaced with a, b, or c to distinguish between fractures in the proximal, middle and distal 1/3, respectively.

	Simple			Wedge		Complex	
	Spiral	Oblique	Transverse	Intact	Fragmentary	Segmental	Comminuted
	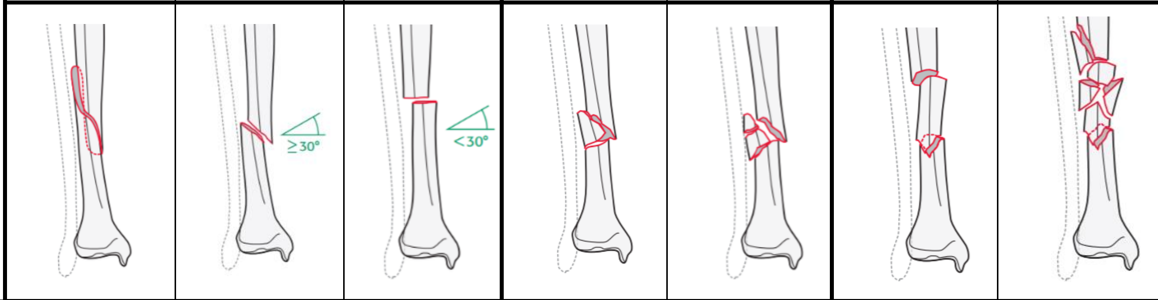						
AO Code	42(12)A1*	42(12)A2*	42(12)A3*	42(12)B2*	42(12)B3*	42(12)C2*	42(12)C3*
Prevalence Ranking	3	1	2	4	5	6	7
Typical Cause	Twisting injuries sustained during sports or during a physical attack	A sharp blow that arises in light of a fall from a considerable height		High energy, traumatic accident, such as a high speed car collision			
	Lower Energy	→					Higher Energy

2.2 PRIMARY INTERVENTION STRATEGIES & HEALING PATHWAYS

All construct configurations may be broadly categorized into one of two subsets, of which the most prevalent and highly regarded is flexible, 'biological' fixation [13]. This provides relative stability by promoting indirect, secondary healing and does not require anatomical reduction, since the fragments need only be approximately aligned. Thus, a bridging intramedullary nail (IMN) or plate may be percutaneously inserted in a swift and straightforward manner, limiting bone exposure, and minimizing surgical trauma [5] (see FIGURE 4). The former involves driving a long cylindrical rod and subsequently fixated internally within the medullary canal via a small breach in the epiphyses of the LB, whereas the latter necessitates fastening the construct either directly upon, or just external to the cortex of the LB.

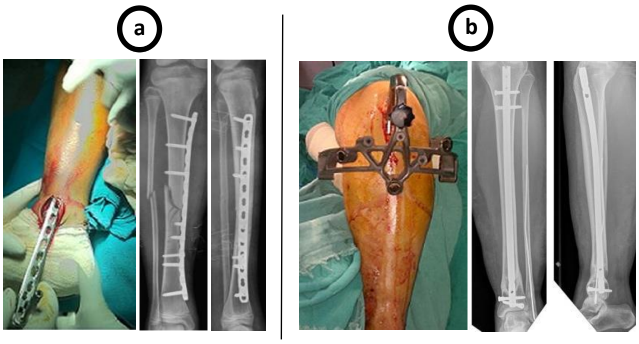

FIGURE 4 | Percutaneous insertion of **(a)** a plate; and **(b)** an IMN. Radiographs of the resulting assemblies are also shown. [14]

Following these types of treatment, the indirect pathway of healing begins with diffusion and proliferation of mesenchymal stem cells (MSCs) within the fracture gap, following haematoma [15]. These MSCs percept mechanical stimuli that determine their differentiation, and constitute the 'bone healing unit' (BHU) [16]. Over time, the BHU evolves through the different stages of reparative osteogenesis (see FIGURE 5), producing a callus of progressively stiffer tissue (granulation tissue, cartilage and finally bone) that can tolerate diminishing magnitudes of mechanical stimuli. It is this dynamic process of healing that embroils construct selection. If overly compliant, the cartilaginous tissue will be unable to reduce the stimuli to below that which can be tolerated by lamellar bone, and the fracture will fail to heal. Conversely, if overly stiff, mechanical stimuli will be greatly suppressed and a meagre volume of callus will form, diminishing its load-bearing capacity and magnifying stress shielding within the system. As a result, either implant loosening or fatigue failure of the construct could arise in advance of a fully unified fracture [13], although in practise surgical intervention prevents these from occurring.

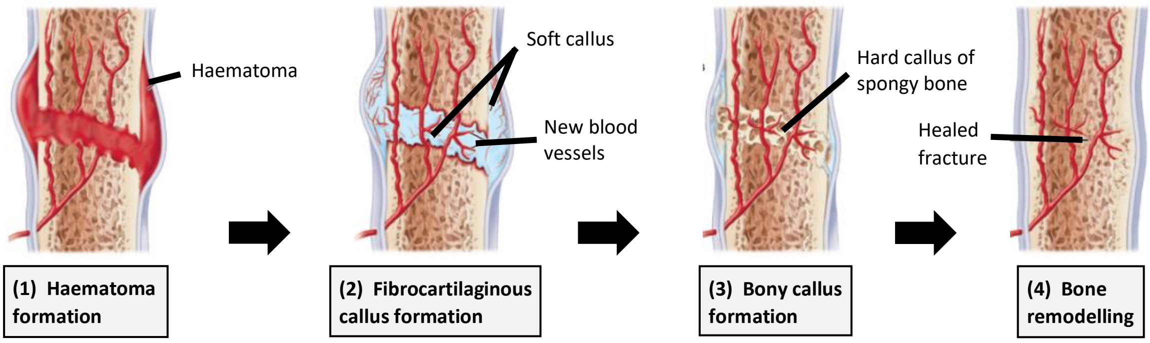

FIGURE 5 | Secondary healing: the four stages of reparative osteogenesis. Adapted from [12].

The other subset of configurations are rigid fixation methods (see FIGURE 6). Here, absolute stability through open anatomic reduction and subsequent compression of the fracture ensures that cortical continuity is re-established to within 0.01 mm, and that the mechanical stimuli are maintained below that which can be tolerated by bone [17]. As such, the bone is simulated as being intact, allowing direct, primary healing to occur through the normal homeostatic remodelling of bone (intramembranous ossification, see FIGURE 7, overleaf). There is great propensity for uneventful, functionally sound repair, should the patient be a young, fit and healthy individual presenting with a simple fracture [18]. However, the surgical installation necessitates much manipulation of the fracture site through an open

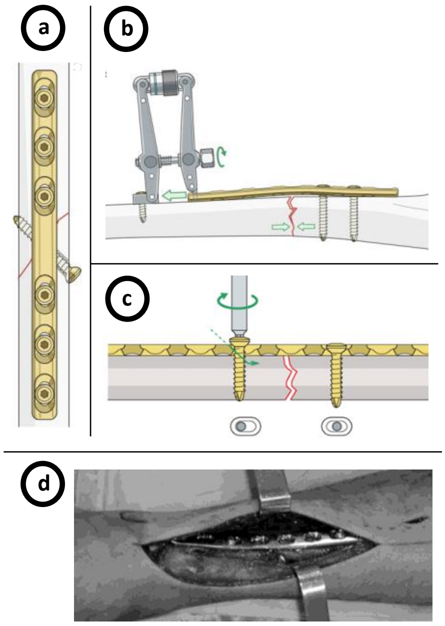

FIGURE 6 | Rigid fixation techniques: **(a)** interfragmentary lag screw with neutralization plate; **(b)** compression plate preloaded by means of an articulated device; **(c)** compression plate preloaded through the eccentric insertion of dynamic locking screws; and **(d)** open anatomical reduction using a dynamic compression plate [18].

incision, compromising its vascularity [13]. Therefore, if these two factors are superposed by any comorbidities [19], [20], or life style aspects [21] of the patient that gravely retard the reparative process of healing, the same ultimate outcome of an overly stiff flexible fixation will ensue. Additional drawbacks include cost, duration and intricacy of the surgical procedure [22]. Furthermore, rigid fixation configurations are incompatible with complex, highly comminuted fractures. Hence, with the exception of intra-articular fractures, for which perfect alignment is critical to restore normal physiological function, they are rarely adopted [13].

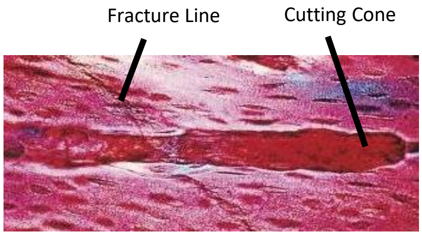

FIGURE 7 | Direct, primary bone healing through intramembranous ossification. Adapted from [13].

2.3 REVISIONARY SURGICAL TECHNIQUES

The need to establish a simple, brisk and cost-effective type of revisionary surgery to treat non-union is apparent. Consequently, surgeons have been experimenting with novel, makeshift alternatives for some considerable time. The findings of a recent clinical study suggest that the additional insertion of one or more interfragmentary percutaneous strain reduction positional screws (PSs), or 'shear pegs', perpendicular to the plane of fracture (see FIGURE 8), as part of an outpatient procedure, is a viable way forward and that it has serious potential to replace the current conventional and traumatic options of exchange nailing and compression plating [23], wherein the old osseointegrated construct is removed and replaced by a more rigid and stable alternative. Nevertheless, this technical trick remains to be numerically verified, meaning great scepticism continues to surround its clinical adoption at present.

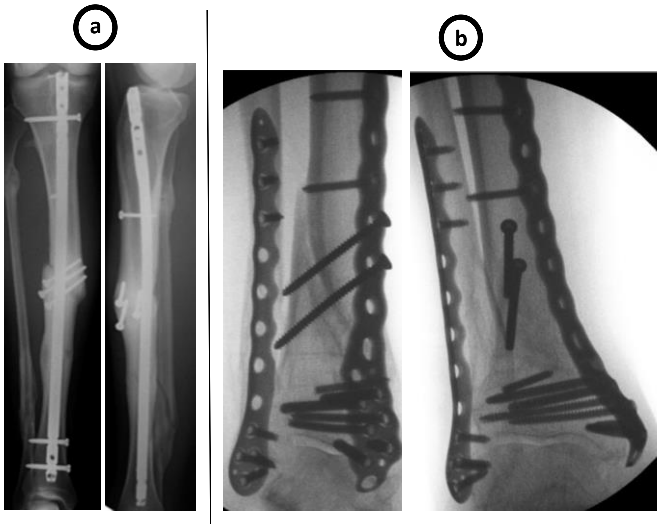

FIGURE 8 | PSRPSs inserted alongside **(a)** an IMN and **(b)** a bridging plate to treat non-unions. Adapted from [46].

2.4 MECHANO-REGULATION THEORIES

It is apparent from sections 2.2 and 2.3 that the magnitude of some sort of mechanical stimulus at the site of an LB fracture can drastically influence its healing pathway, in one way or another. Mechano-regulation (MR) theories, which have been extensively researched in the field of bone tissue engineering for a number of years, demystify this phenomenon by relating the magnitude of a well-defined stimulus to the development of a specific tissue phenotype of a given stiffness.

Three main MR theories exist, with the most intuitive taking inter-fragmentary strain (IFS) as the stimulus for cell proliferation. This is defined as the relative motion, or interfragmentary motion (IFM), of the fracture faces over the width of the fracture gap, g:

$$IFS = \frac{IFM}{g} \tag{1}$$

Such simplicity has obvious benefits, yet these are achieved to the detriment of accuracy. This is in stark contrast to bi-phasic MR theory, which sees the stimulus, S, regarded as a weighted summation of deviatoric strain, ε', and fluid flow velocity U (µm/s), across a small, localised region of callus tissue (see Equation 1). It is thus considered superlative at capturing the true mechanics behind bone remodelling [24].

$$S = \frac{\varepsilon'}{3.75} + \frac{U}{3} \qquad where \qquad \varepsilon' = \frac{2}{3}\sqrt{(\varepsilon_1 - \varepsilon_2)^2 + (\varepsilon_2 - \varepsilon_3)^2 + (\varepsilon_3 - \varepsilon_1)^2} \tag{2}$$

Finally, ε' may be regarded a stimulus in its own right, as part of deviatoric strain MR theory. This is popular amid research since it is known to strike an reasonable balance between the gross inaccuracy of IFS theory and the difficulties associated with measuring or modelling U [25].

The stimulus-tissue stiffness mappings associated with each of the above theories are summarised in TABLE 2, below, together with a colour code system that will be called upon in this report.

TABLE 2 | Lower and upper bounds of inter-fragmentary strain, deviatoric strain and bi-phasic stimuli that can be tolerated by each of the seven main types of tissue associated with secondary healing of fractures. Typically one performs linear interpolation between the given magnitudes of stimuli and tissue stiffness so as to acquire a continuous mapping [25].

Tissue Type		Granulation Tissue	Fibrous Tissue	Immature Cartilage	Mature Cartilage	Immature Bone	Intermediate Bone	Mature Bone
Colour Code								
Tissue Stiffness (MPa)		0.2	5	10	500	1000	2000	6000
Stimulus	IFS (%)	100	10		2			1
	ε' (%)	100	5		2.5	0.05	0.005	
	S	100	3		1	0.267		0.01

2.4 PREVIOUS FINITE ELEMENT WORK

Numerous FE studies have investigated how the material properties [26], [27], geometry [28]–[32] and screw configuration [33]–[35] of flexible fixation constructs influence the initial, post-operative magnitude of IFS for simple fractures of differing obliquity and gap size [36], in the absence of callus.

On the contrary, few have exploited the more advanced MR theories to numerically evaluate the impact such variables have on the dynamic process of healing [24], [25], [37]–[42].

Similarly, only the minority consider physiological muscle loads, which have been shown to drastically influence the biomechanical performance of constructs [43], [44]. Moreover, previous work is almost exclusively limited to variations in a single variable, giving rise to poor continuity and contradictions amidst literature [45], [46]. Finally, studies are yet to base their analyses on constructs that are currently circulating within the UK's National Health Service (NHS), further squandering the ability for findings to the make a lasting impact on clinical practise.

2.5 PRELIMINARY SPECIFICATION FOR THE BASE MODEL

IM nailing is generally perceived superior to plating [47] due to its lower risk of infection, and preservation of periosteal blood supplies [48]. Furthermore, simple, single line, mid-shaft fractures of the tibia are most susceptible to non-union [36]. Therefore, a comprehensive, stand alone, MR FE parametric study that accurately and numerically quantifies the effect of simple fracture geometry (obliquity and gap size), primary intervention strategy (nail diameter and screw positioning), degree of weight bearing, and the use of percutaneous screws as an alternative to the revisionary technique of exchange nailing, on the mechanics behind the healing of LB fractures treated with the NHS's Stryker T2 tibial nailing system, is needed. This will maximise the number of LB fracture admission cases wherein surgeons can directly relate to and confide in the work of this study to confidently inform the treatment strategy.

3 MODEL DEVELOPMENT & PRIMARY SET-UP

As a novice FE analyst, the author adopted a highly scalable approach to model development so as to enable ones confidence and proficiency in using FE software to be incrementally bolstered, and the intricacy of an elementary working model to be slowly evolved into one that that may be perceived superior to others in its field. This chapter will outline its primary set-up, clearly detailing and justifying all decisions and assumptions made prior to its validation and fine tuning.

3.1 CAD MODELLING

The virtual construction of an IMN assembly is challenging, awkward and arduous due to the arbitrary morphology of its constituents. For the most part, SOLIDWORKS was used as the medium for this painstaking process, the broad details of which are described below.

3.1.1 TIBIA

The simplified concentric cylinder FE models of bone that are scattered amidst literature for use as part of elementary studies are incompatible with an investigation into the performance of percutaneous screws as a revisionary surgical technique (see FIGURE 9) [1]. Hence, the author had little choice but to reconstruct a tibia of life-like geometry. An artificial Sawbones 3401 left tibia, which is marketed as being typical of that of a medium sized, middle aged female adult, was adopted in preference to a real, patient-specific case, since the latter would have necessitated ethical approval, rendering completion of the project infeasible in the pressing timescales of a final year project.

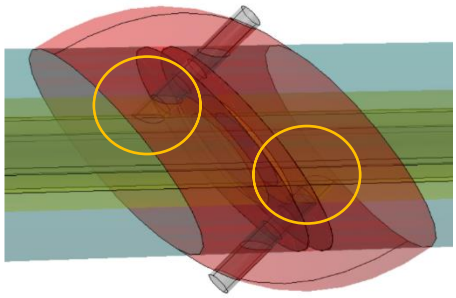

FIGURE 9 | Percutaneous screws cannot be inserted perpendicular a fracture plane that constitutes a concentric cylinder model of bone without breaching the canal within which the nail is situated. Trabecular and cortical bone is coloured yellow and turquoise, respectively.

The bone was initially reconstructed within Geomagic Design X, starting from cloud point data derived from a CT scan, whose individual images each had a slice thickness of 0.4 mm and a pixel size of 0.441 mm on a 512 × 512-pixel frame. This software converted the data into an STL, enabling the resulting geometry to be amended until void of artefacts, smoothed, and analytically surfaced into a CAD interface compatible part, using non-uniform rational B-spline (NURBS) patches.

SAWBONES 3401 tibias have no medullary canals, yet such features of LBs are pivotal to the performance of an IM nail, dictating its orientation and stability within the bone. As such, one had to be manually inserted with great diligence, within SOLIDWORKS. Tibial medullary canals are approximately straight, with their longitudinal anatomical axis coinciding with that of the tibia itself [49]. In order to determine the latter, a right handed Cartesian coordinate system was defined upon the centroid of the tibio-calcaneal articular surface: the z axis was made to penetrate the most proximal point on the intercondylar eminence, whilst the y axis was orientated frontally, being placed perpendicular to a line through the most medial point on the medial malleolus and the most lateral point on the fibular notch. The x axis was orientated medially (see FIGURE 10) [50]. A lofted cut was then taken along the resulting z axis, through scaled down profiles of the cortex, to return a canal of shape and size typical of real tibias. Following this, the meagre volume of trabecular bone that remained within the diaphysis was omitted from the model, since such an operation would facilitate meshing and hasten the computation of FE analyses, all whilst having a negligible impact on the bone's structural integrity [50]. Full dimensional details of the resulting intact tibia feature in APPENDIX A for the perusal of the interested reader.

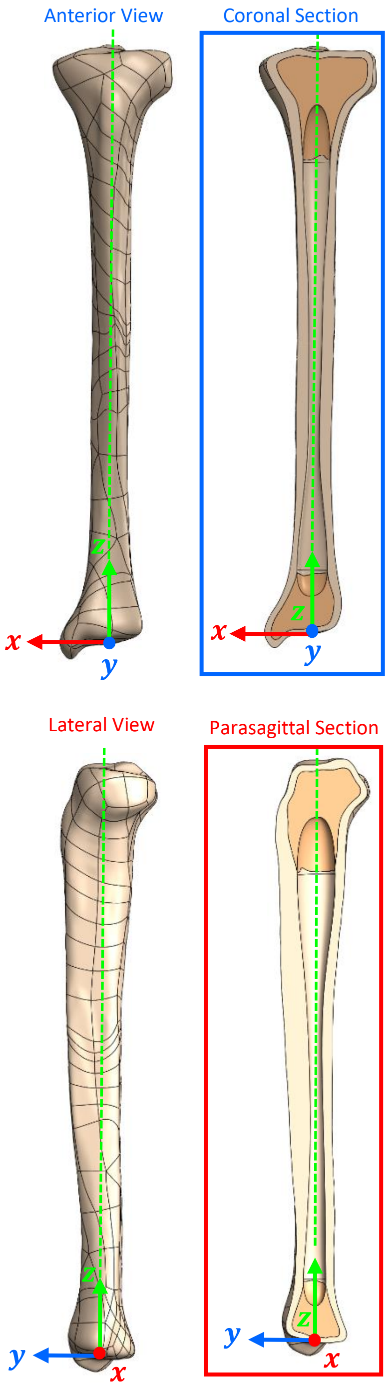

FIGURE 10 | Anterior and lateral views of the modified intact Sawbones tibia used in this study, as well as its associated coordinate system, which shall be frequently referenced in subsequent sections of the report.

Next a virtual osteotomy was performed at the mid-shaft location to simulate a simple, oblique fracture of AO classification 42A2b. The cut had a medial to lateral angulation of $\theta_{ML} = 45°$ upon the coronal plane, as well as an anterial to posterial angulation of $\theta_{AP} = 45°$ upon a parasagittal plane, which shall hereafter be referred to as a $45ML - 45AP$ fracture, or a $\theta_{ML}ML - \theta_{AP}AP$ fracture in the most general sense (see FIGURE 11a, overleaf). This geometry was chosen, as it is commonly reported as being the most prevalent. Furthermore, the size of the fracture gap, defined as the distance between the fracture faces along their common normal (g_n, see FIGURE 11b, overleaf), was chosen to be 3 mm, as is typically done in this field of research.

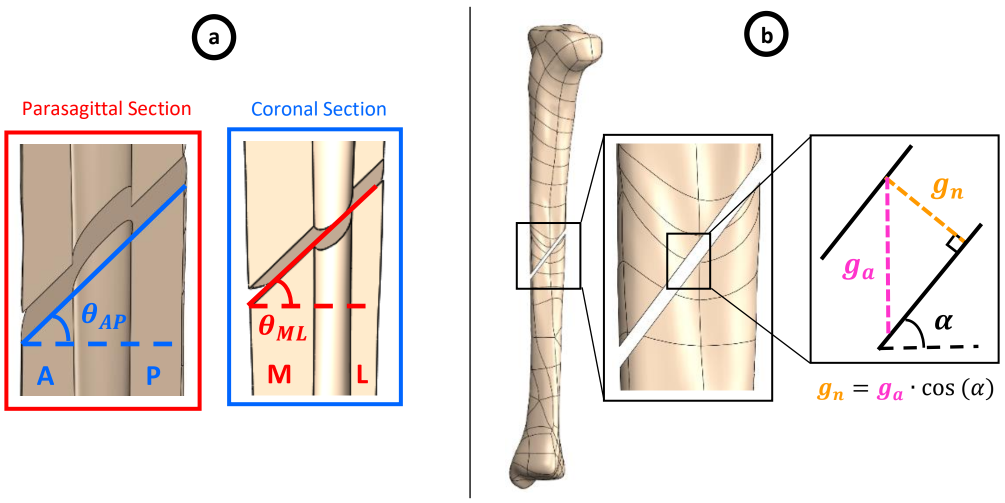

FIGURE 11 | Fracture site geometry terminology. (a) Definition of angles of obliquity, θ_{ML} and θ_{AP}. (b) Definition of the normal gap width g_n and its relation to the width of the gap in the axial direction, g_a.

3.1.2 CONSTRUCT

The nail was modelled in a more conventional, less subjective manner, using dimensions reported within the Stryker T2 Standard Tibial Nail Catalogue [51], for the part of overall length that best suited that of the Sawbones tibia, and of outer diameter of 10 mm, as this size is known to be suitable for the majority of patients [51]. Again, an engineering drawing of the part (1823-1034S) has been supplied in APPENDIX B, should one desire to learn its exact dimensions.

As for its accompanying 5mm 1896-50 fully threaded locking screws, these were modelled as plain, truncated 5 mm cylindrical pins with neither heads nor threads, since such intricate features would have rocketed the computational demands of an already elaborate and convoluted FE model, far beyond that which any shared high performance computing service could accommodate. Four were created in total and subsequently inserted within the nail to give the 12-46 configuration outlined in FIGURE 12, below. This was done in light of various recommendations detailed within the manual.

FIGURE 12 | CAD model of the IMN annotated with the screw hole numbers that will be used to define a given screw configuration in subsequent sections of the report.

3.1.3 CALLUS

Substantial time and effort was also dedicated to the modelling callus, which was carefully designed so as to ensure that a larger material volume was present in regions further from the nail's axis, wherein material elements are disposed to greater mechanical stimuli. This was achieved by lofting the part to a height of 141 mm, between two cortical cross-sections, each parallel to, and equidistant from, the fracture face of one of the fragments. Guide curves were used with a radius of curvature, y, directly proportional to the distance of their root from the nail, x (see FIGURE 12) and the constant of proportionality was set equal to the most prevalent callus index currently being observed clinically (1.4, [53]).

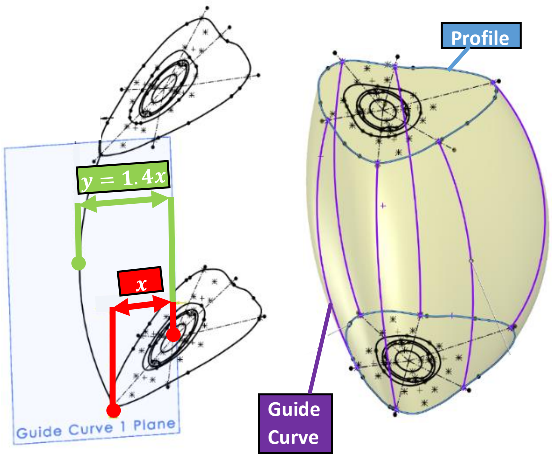

FIGURE 22 | CAD modelling the callus through a loft between two cortical cross sections of the tibia.

3.1.4 ASSEMBLY

Following completion of all constituent parts, the centreline of the nail's long, central portion was made to coincide with that of the tibia's canal (z axis), its proximal bend was set to point towards the anterior tubercle, and its distal tip was positioned 20 mm above the distal epiphysis. The tibia was then virtually reamed along the path line of the nail, to a diameter 1mm greater than that of the nail. Moreover, screw holes were cavitated within the tibia using the plain, cylindrical pins that had already been pre-located within the nail, and the callus was cavitated using the tibia. Finally, the nail was plugged proximally using a +10 mm x 11.5 mm 18222-00105 end cap, which is used to avert ingrowth and thus infection post-operation.

This method of assembly was considered to best replicate the outcome of the true operative technique adopted by surgeons in theatre [54], [55], with the largest simplification being the absence of a three point nail-bone contact, as well as any pre-load within the nail. Still, the impressive straightness of tibias means that these phenomena are readily neglectable for the IM nailing of such bones. This is in contrast to femurs, which can have a substantial camber, and so these same simplifications may severely compromise all findings of an investigation. A statically locked and reamed assembly was also realised over a dynamic or unreamed set-up, as although its superiority remains a subject of great controversy from a mechanical perspective [56], such

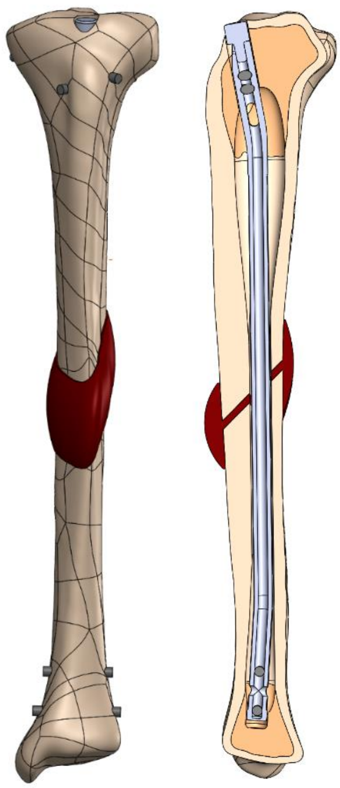

FIGURE 33 | Final CAD assembly of the base model.

assemblies are almost always preferentially adopted by surgeons, due to their comparative ease of surgical implementation [57], [58].

3.2 MATERIAL PROPERTIES

Following CAD modelling of the assembly, all of its constituents were imported within ABAQUS, before assigning a set of material properties to each.

It has been experimentally shown that the assignment of isotropic properties to cortical bone mass as part of FE analyses suffices when the bone is subject to simple 3 point bending [9]. However, the fidelity of such an approximation is known to break down rapidly for other more convoluted loading regimes that impart a state of torsion with the bone [59]. In such cases, only a more computationally expensive orthotropic or heterogenous description will suffice. With the use a homogenous artificial Sawbones tibia rendering the latter infeasible, the former was thus decided upon for use in this study. Similarly, all trabecular bone was regarded orthotropic, as although the anisotropy of this tissue type is adequately low for an isotropic approximation to be broadly valid, several authors have reported only a minor saving in computation cost through making this simplification.

The material assignment for the rest of the parts proved a much simpler task, since these are consistently perceived isotropic within literature [59]. More specifically, the callus was thought to comprise granulation tissue, as studying its healing potential at the onset of reparative osteogenesis, when the assembly is in its least stable state, enables one to delineate the superiority of a given setup as compared to another in less ambiguous fashion. It is also the incipient stage of healing that sets the principal direction of the healing pathway. Bi-phasic properties were at first not considered due to the fact that uni-phasic ε' MR theory is generally accepted as a good alternative to bi-phasic MR theory (see section 2.4) for evaluating a callus' healing potential. Finally, the screws and nail were taken to be titanium, in accordance with the Stryker manual [4].

The properties that were assumed for each of the above materials are outlined in TABLE 3, below.

TABLE 3 | Full breakdown of all material properties comprising the base model.

Material	Ref.	Part	Young's Modulus			Poisson's Ratio			Shear Modulus		
			E_r	E_θ	E_z	$v_{r\theta}$	v_{rz}	$v_{\theta z}$	$G_{r\theta}$	G_{rz}	$G_{\theta z}$
Cortical Bone	[1]	Tibia	8500	6900	18400	0.141	0.065	0.099	2400	4900	3600
Trabecular Bone	[2]	Tibia	676	968	1352	0.3	0.3	0.3	370	505	292
Granulation Tissue	[3]	Callus	0.2			0.167					
Titanium 6AL-4V	[4]	Construct	114000			0.33					

3.3 LOADING & BOUNDARY CONDITIONS

Two potential routes for loading the assembly were carefully contemplated, namely a simplified case, wherein the tibia is strained uniquely through its two proximal epiphyseal condyles, and a more realistic physiological case, using which muscle forces would be also accounted for. The latter was ultimately chosen because aside from their capability to allow relative movements in joints, muscles play a major role in counteracting shear and bending loads, which would otherwise culminate in a gross overloading of the LB, as compared to reality [50].

The largest deformation of a tibia's mid-shaft arises at the second peak in ground reaction forces during the phase in gait between 'heel off' and 'toe off' (45% of the whole gait cycle, see FIGURE 14). Hence, this single instant in gait denotes a worst routine loading case scenario for a mid-shaft fracture construct, and is why it was selected for all analyses in the present study[50].

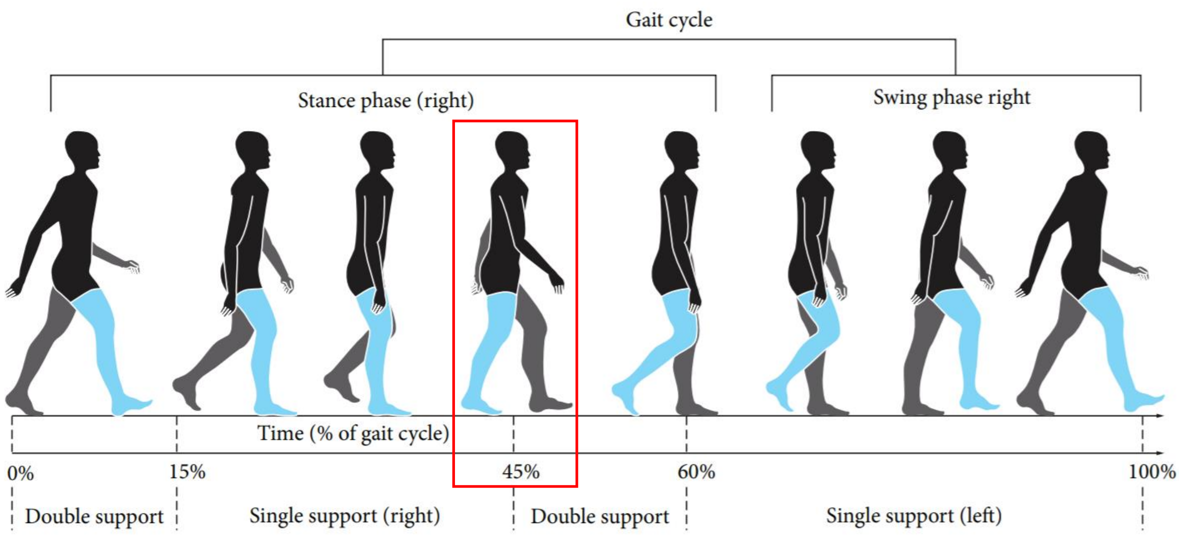

FIGURE 14 | Breakdown of the different instances in time in the human gait cycle. The instance used in this study is highlighted in red [58].

The modelling of this loading regime began by acquiring tibial muscle concentrated force data for an 80 kg individual from [50], before scaling it to the size of the Sawbones tibia used as part of this investigation and transforming it to the coordinate system defined in FIGURE 10 of Section 3.1.1 in this report (see TABLE 3, overleaf). A python script was then written within the commercial finite element software package, ABAQUS, to compensate for the slight disparity in attachment locations that arises due to minor differences in bone morphology between the two studies. This applied each muscle force at a surface node of the Sawbones' cortex closest to its prescribed co-ordinate attachment location (see FIGURE 15, overleaf).

TABLE 4 | System of physiological muscle (m.) and ligament (lig.) concentrated force magnitudes, and their attachment coordinates, that have been employed in all analyses. Tibial muscles and ligaments that are known to be inactive at 45% gait are also detailed for the sake of completion and are highlighted in blue. The knee and ankle joint contact forces may be considered to be a summation of the vectors of the resultant joint force and the forces of those muscles and ligaments crossing. [50]

No.	Name	Force (N)			Attachment Location (mm)		
		x	y	z	x	y	z
-	Gracilis m.	0.0	0.0	0.0	-9.4	31.6	319.3
-	Sartorius m.	0.0	0.0	0.0	-9.2	28.4	308.1
-	Semimembranosus m.	0.0	0.0	0.0	18.2	-22.8	359.0
-	Semitendinosus m.	0.0	0.0	0.0	36.4	5.1	361.6
1	Iliotibial tract I	8.4	-8.1	58.7	-37.5	-19.0	354.4
2	Iliotibial tract II	61.7	-93.3	279.3	-27.0	-26.0	355.0
3	Quadriceps femoris m.	31.4	13.0	290.8	-18.5	33.3	338.6
-	Extensor digitorum longus m.	0.0	0.0	0.0	-12.8	3.0	102.6
-	Extensor hallucis longus m.	0.0	0.0	0.0	-14.5	5.2	252.6
-	Flexor digitorum longus m.	0.0	0.0	0.0	-3.7	-7.7	269.5
4	Tibialis anterior m. I	-37.1	16.5	-314.0	-9.5	-4.7	241.3
5	Tibialis anterior m. II	-51.4	24.8	-183.8	-9.5	-7.3	122.6
-	Tibialis posterior m.	0.0	0.0	0.0	8.5	-3.4	240.9
6	Soleus m.	45.1	-60.5	-650.6	-14.4	-7.1	318.3
7	Ant. tibiofibular lig.	106.6	-126.9	-54.4	-10.6	-7.0	0.9
8	Ant. cruciate lig.	-97.3	83.8	39.4	4.8	9.9	374.2
9	Deltoid lig.	-9.3	43.0	15.0	15.8	-1.4	-0.3
-	Post cruciate lig.	0.0	0.0	0.0	-5.7	-5.7	372.1
-	Knee	-205.9	222.6	-1464.3	1.9	1.4	372.0
-	Ankle	148.0	-115.0	1983.9	-0.6	0.8	0.4

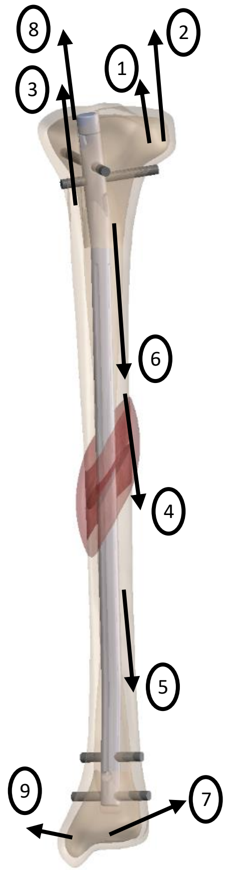

FIGURE 15 | Visual representation of the approximate muscle and ligament force magnitudes and directions used for this study, together with their attachment locations.

TABLE 4, above, also features transformed joint contact force data lifted from [50], yet these were not applied to the model in their raw, concentrated form, since they were regarded as a much too simplistic representation of the manner in which they are applied in reality.

Typically, surgeons advise their patients to bear 50% of their bodyweight (BW) following the insertion of an intramedullary nail. Consequently, the knee contact force data was first scaled down by a factor of two to best replicate the load magnitudes associated with such scenarios. 60% of this load was subsequently assigned to the medial condyle and applied as a parabolic, tractive hertzian contact distribution of specified direction to an elliptical patch of size and shape thought to be representative of the region occupied by articular cartilage through which the load is truly borne. The process was then iterated for the application of the remaining 40% of the knee joint load to the lateral condyle [50] and is summarized in greater detail in FIGURE 16 and TABLE 5, overleaf.

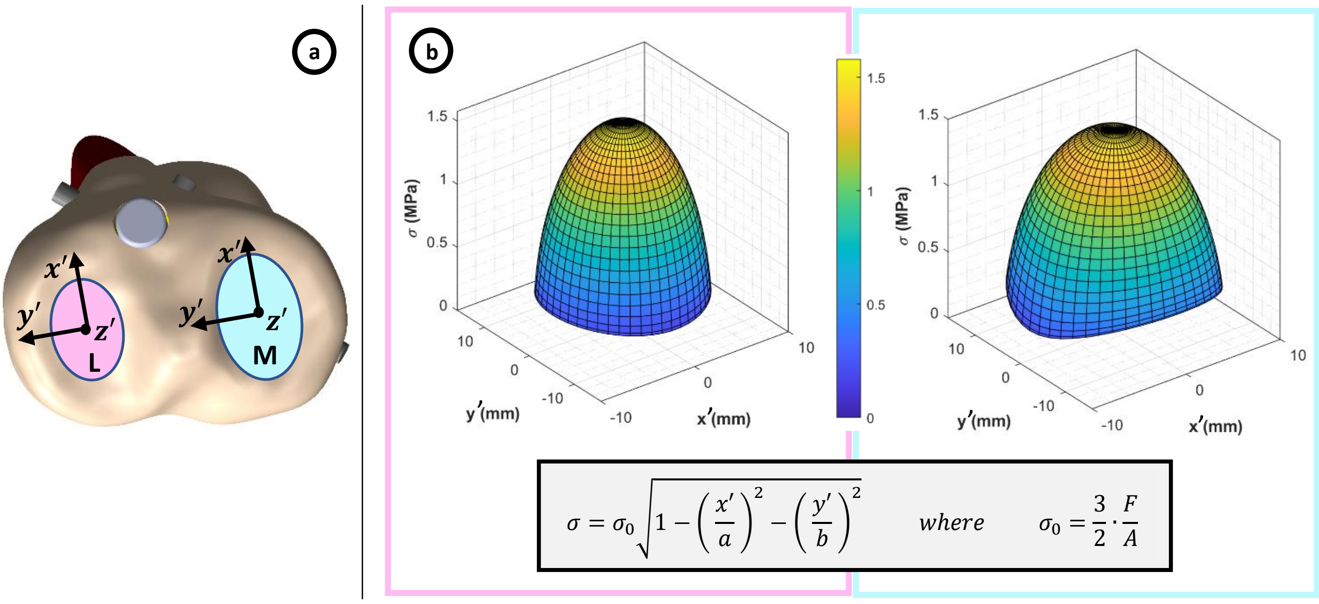

FIGURE 16 | Schematic illustrating the manner in which the knee joint contact loads were applied to the FE model. (a) A local cartesian coordinate system was situated upon the centroid of each elliptical loading patch, with their x' and y' axes coincident upon the a and b semi width axes of each ellipsis, respectively. (b) Visual representation of the applied parabolic, tractive hertzian contact distributions, although it should be noted that their directional components have been neglected here so as to avoid clouding the clarity of the relative magnitudes of each distribution.

TABLE 5 | Qualitative summary of all numerical data used to compute the medial and lateral load patch distributions.

Parameter	Elliptical Semi-widths		Area	Load				
Symbol	a	b	A	F_x	F_y	F_z	F	σ_0
Unit	mm		mm^2	N				MPa
Medial	9.1	15.7	448	-618	66.8	-439.3	448.6	1.501
Lateral	7.6	12.0	285	-41.2	44.5	-292.9	299.1	1.576

The ankle joint reaction force reported in TABLE 4 was similarly modified in magnitude to reflect the reduced knee joint load imparted upon the assembly, yet this time applied as a uniformly distributed tractive force across an area thought to be representative of the proximal profile of an adjacent, broadly flat talus [50]. Furthermore, all degrees of freedom associated with three nodes around the periphery of this area were fixed to prevent rigid body motion (see the tables and figures below).

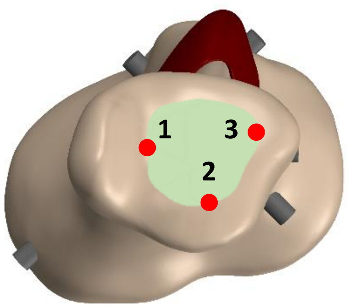

FIGURE 17 | Schematic of the ankle load patch and the location of each BC node.

TABLE 6 | Numerical data associated with the computation of the ankle joint reaction load.

Parameter	Symbol	Unit	Ankle
Area	A	mm^2	554
Load	F_x	N	45.0
	F_x		-3.69
	F_x		1251.8
	F		1252.6
	σ	MPa	2.259

TABLE 7 | Position of each BC node with respect to the coordinate system defined in section 3.1.1 of this report.

Node No.	Co-ordinates		
	x	y	z
1	-1.8	-11.0	0.0
2	-13.1	9.2	4.4
3	12.9	7.0	0.3

Once all loads had been set up, they were made to be ramped linearly over a step of time period 1 s as part of a static, non-linear analysis using ABAQUS Implicit. A small energy dissipation fraction of 0.01 was also defined for the purpose of stabilizing the assembly prior to the nail initiating contact with the tibia. This was ramped down linearly over the step to zero in the final increment so as to diminish its influence on the final findings of this study.

3.4 CONTACT SETTINGS

For one to obtain numerical data of the highest fidelity from an FE simulation, all part geometry must be accurately modelled with friction and 'hard' normal contact behavior, wherein no interpenetration of the contacting bodies is allowed and infinite contact pressures are permitted. However, as was touched upon in section 3.1, the immense computational expense coupled with this approach when applied to large, threaded assemblies renders its adoption inviable in this study. Instead, all threads have had to be neglected and a compromise accepted [57]. Still, a tactful, artificial manipulation of the contact settings within the FE solver could act to curtail the severity of this compromise, if done correctly.

All previous IMN FE studies have treated both the screw-bone and screw-nail contacts as *tied*, or *bonded*, interfaces, declaring that this set-up best models the interlocking of two threads. However, the present author postulates that this is false for two main reasons. Firstly, a selection of these studies report construct peak stress magnitudes in excess of 1 GPa when it is subjected to normal bodyweight loading, yet no cases of gross yielding or complete ductile failure of the construct are observed clinically. Secondly, four recently published state-of-the-art FE plating studies acknowledge that tied contacts render an LB fracture assembly much too stiff, and thus resort to an alternative strategy for modelling screw contacts. The approach involves releasing and 'softening' either one of the screw-nail and screw-bone interfaces, permitting an accurate assessment of the mechanical performance of the freed regions.

In light of the above, three small pilot studies were carried out in a bid to establish a novel, accurate, and reliable method for modelling *both* interfaces within an IMN FE assembly, since *both* of these can influence the selection of an optimal construct configuration for a patient. This was done in the context of a basic fractured concentric cylinder bone, fixated by means of a locked plate, in part due to the complexity and size of the base model, which renders it impractical for experimental trial and error, but also because there is a far vaster body of research, as well as clinical findings, surrounding locked plates. These would grant a quantitative assessment of the validity of the novel technique, prior to its direct propagation across to the base model.

3.4.1 PILOT 1: CONCENTRIC CYLINDERS, TIED CONTACTS & LOCKED PLATING

As a starting point, the most basic long-bone fracture fixation FE study reported within reputable literature was replicated to demystify the issue of tied contacts [58]. This saw an obliquely fractured concentric cylinder composite of isotropic trabecular bone and anisotropic cortical bone, fixated with a locked stainless steel plate, uniformly and axially loaded with 10% bodyweight (BW), and modelled alongside threadless screws that were 'tied' to their respective interfaces. After running the analysis, the IFS was computed as a function of radial distance, r (see FIGURE 18).

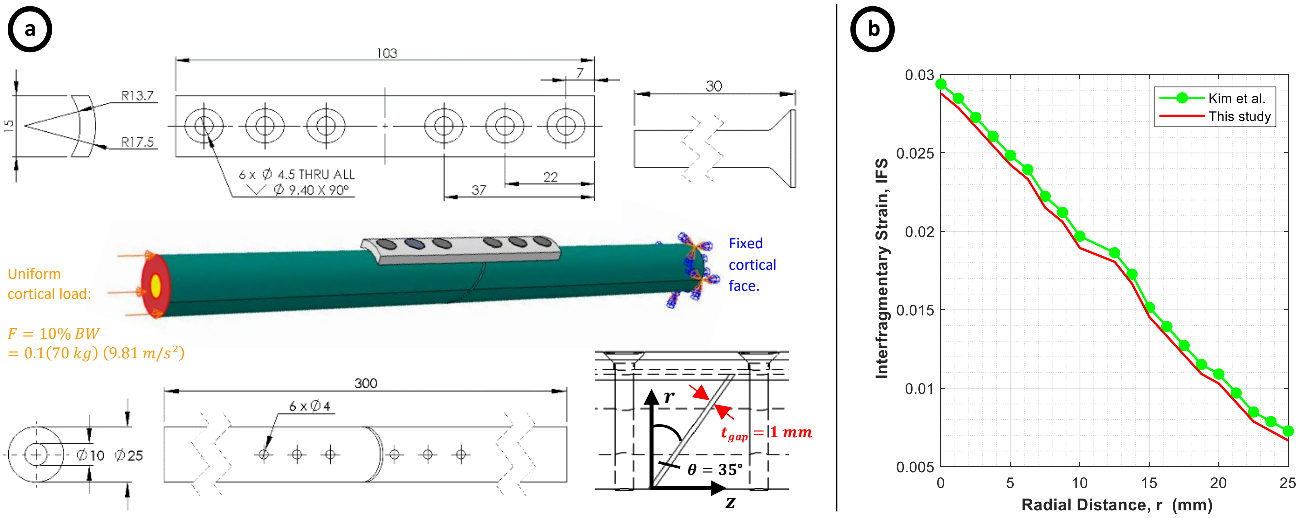

FIGURE 18 | (a) Loads, boundary conditions and important dimensional details of all parts constituting the elementary FE model; and **(b)** a plot of IFS as a function of r for validation purposes. The small discrepancy may be considered to arise uniquely from the use of overly stiff tetrahedra, rather than hexahedra, in the present study. These were adopted to avert the need for a tedious and laborious bottom-up meshing strategy.

Close correspondence between the acquired data and that presented in [58] confirmed that the model had been set up and post-processed correctly. However, the results were still spurious in two respects. Firstly, the modest IFS magnitudes of approximately 2% suggested that the system was too stiff to stimulate sufficient callus formation for healing to occur, despite the fact that the findings of innumerable clinical studies show that similar configurations promote complete consolidation of an abundant callus volume [59]. Secondly, stress singularities superposed and concealed the true stress fields at the periphery of each hole, meaning the likelihood of loosening, cut-out, yielding and fatigue failure of the screws and plate could not be quantified with any reasonable certainty (see FIGURE 19). These findings are direct proof that tied contacts are an ineffective way of modelling

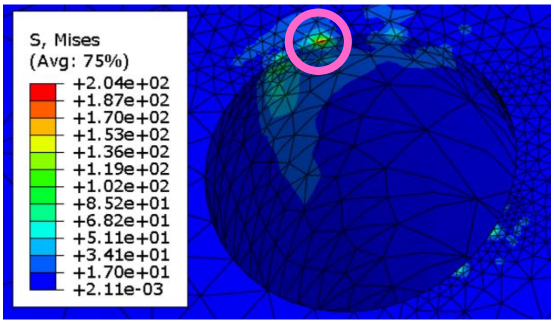

FIGURE 19 | A stress singularity is highlighted in pink and is characterised by non-convergence of the solution with refinement of the mesh.

screw interfaces and fortified the author's hypothesis. Hence, a second investigation was launched to explore superior substitutes for this basic formulation.

3.4.2 PILOT 2: PURE PENALTY 'SOFTENED' CONTACTS

Each of the four studies that release one of the screw interfaces employ Pure Penalty, 'softened', frictional contacts at the free faces [57]. Here, the normal contact force, F_N, is made proportional to an artificial overclosure of the two mating surfaces, $x_{penetration}$, by means of a hypothetical spring of stiffness K_N positioned between them:

$$F_N = K_N \cdot x_{penetration} \tag{4}$$

For advanced applications, F_N may be specified by the user to precisely account for the compliance of a suppressed thread, for example, or to hasten the acquisition of a converged solution by smearing the stress distribution over a given area [60], [61]. Piecewise-linear [62] and exponential [63] alternatives to Equation 4 may also be defined. Alternatively, a normal stiffness factor, fkn, can be specified [64]:

$$K_N = K_{N_{DEFAULT}} \cdot fkn \tag{5}$$

All of these formulations have been called upon within literature, but with very different settings in each case (see the above citations). Hence, a basic analytical model was set up to discern the sensitivity of construct compliance to these settings (see FIGURE 20). The results (see TABLE 8) revealed that careful tuning of the contact parameters to either experimental data or a threaded screw sub-model will ultimately be necessary if truly accurate displacements are to be computationally acquired. However, for simplicity, their values were arbitrarily lifted from past studies at this stage, since this would suffice as a means of ensuring all the shortcomings of 'tied' contacts could be resolved using the sophisticated technique.

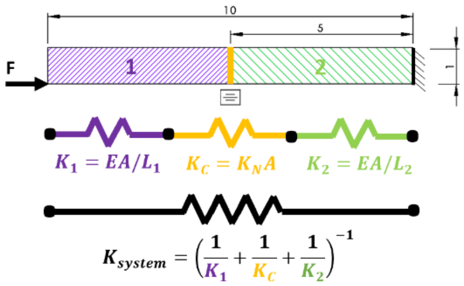

FIGURE 20 | Soft contact model, wherein an axial, compressive, concentrated load of F=10 kN is applied to the free end of an axisymmetric stack of two cylindrical steel rods, and an fkn value is defined at their interface. The theoretical displacement of the loading face can be manually computed by likening the system to the series combination of 3 springs.

TABLE 8 | Results of the investigation defined in FIGURE 7. The compliance of the system is significantly incremented for low contact stiffnesses. The close agreement between theoretical and computational data signifies that the analytical model described by (2) replicates the actual algorithm being implemented by the FE software.

fkn	1	10^{-1}	10^{-2}	10^{-3}
K_N (N/mm^3)	4 x 10^7	4 x 10^6	4 x 10^5	4 x 10^4
$\Delta x_{Analytic}$ (mm)	0.63694	0.63980	0.66845	0.95493
Δx_{FEM} (mm)	0.63723	0.64009	0.66873	0.95512
Error (%)	0.05	0.04	0.04	0.02

Further improvements saw the plate and screws remodelled with more realistic geometry, and the inclusion of a callus comprising granulation tissue, bringing the model closer to that of the complex IMN base case. Moreover, 'springs' were inserted tangential to the screw interfaces to grant a quantitative assessment of the proximity to axial screw loosening and pull-out [61]. Their points of attachment were strategically placed in the least critically stressed locations of each part, far from the regions of interest (ROIs), since it was thought that this would allow the stress singularity artefacts that they impose on the system to be safely ignored (Saint-Venant's principle [65], see FIGURE 21). Finally, the ROIs were automatically adaptively re-meshed, subject to a uniform 5 % error in the von Mises stress, σ_{VM}, and the analysis was rerun, before being iterated for loads of 100% BW, as well as transverse fractures - the results proved promising.

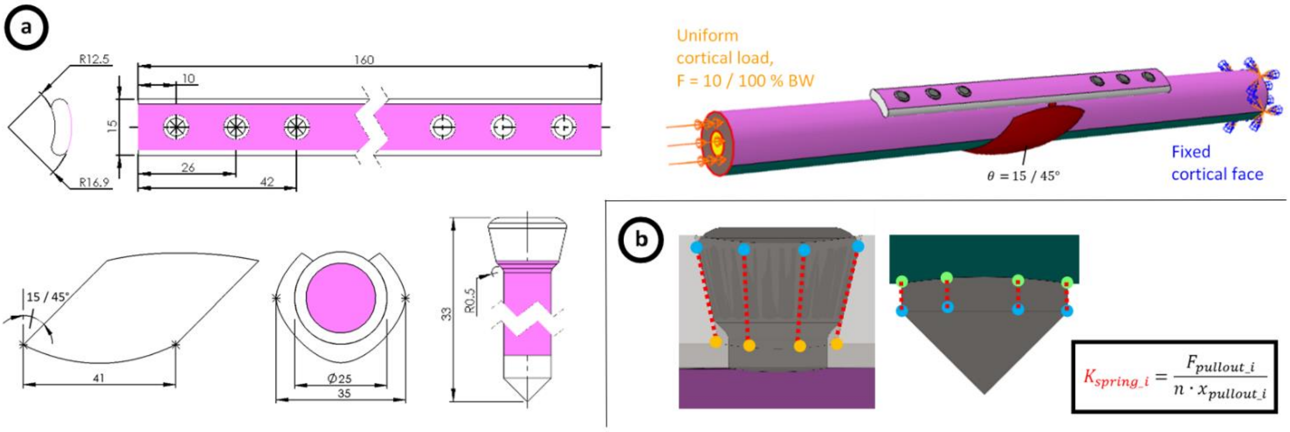

Figure 21 | (a) Modifications made to the geometry and loading conditions defined within the elementary model. The ROIs are highlighted in pink. **(b)** Location of spring attachment points on the screws (blue), plate (orange) and bone (green), at the screw-plate (left) and screw-bone (right) interfaces. $n = 8$ springs were evenly distributed around each interface, and their stiffnesses were derived from experimental pull-out data circulating within literature [54]. K_{spring_i} , $F_{pullout\_i}$ and $x_{pullout\_i}$ denote the spring stiffness, ultimate screw pull-out load and the ultimate screw pull-out displacement at interface i, respectively.

To hasten post-processing, IFS distributions were not computed. Rather, the maximum axial and shear interfragmentary motions (IFMs) were ascertained for each case (see FIGURE 22). From these, one could crudely infer that the IFS magnitudes had increased by a factor of 10, which is aligned with literature in which 'ties' have been experimentally shown to be approximately 8 times too stiff for locked plate constructs [60]. The data also verified the collaborating surgeon's hypotheses that axial

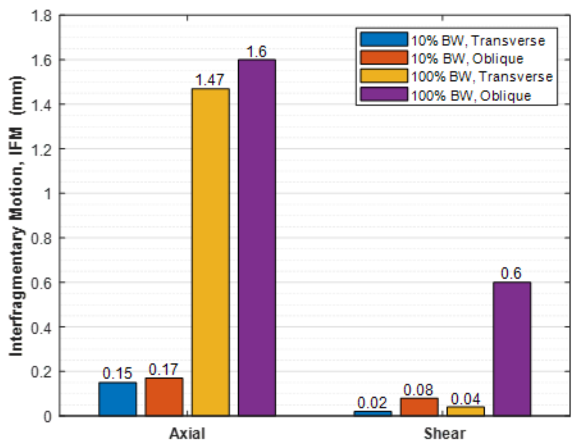

FIGURE 22 | Influence of fracture obliquity and load magnitude on the maximum axial and shear IFM, defined as relative fracture face displacement in the proximal-distal and medial-lateral directions, respectively.

IFM scales linearly with applied load, and that fracture obliquity has a marked effect on shear IFM only. Furthermore, all stress distributions could now be evaluated with accuracy. These were all shown to be valid in light of their close agreement with analytical calculations, and with clinical data (see FIGURE 23, and FIGURES 24 and 25 overleaf).

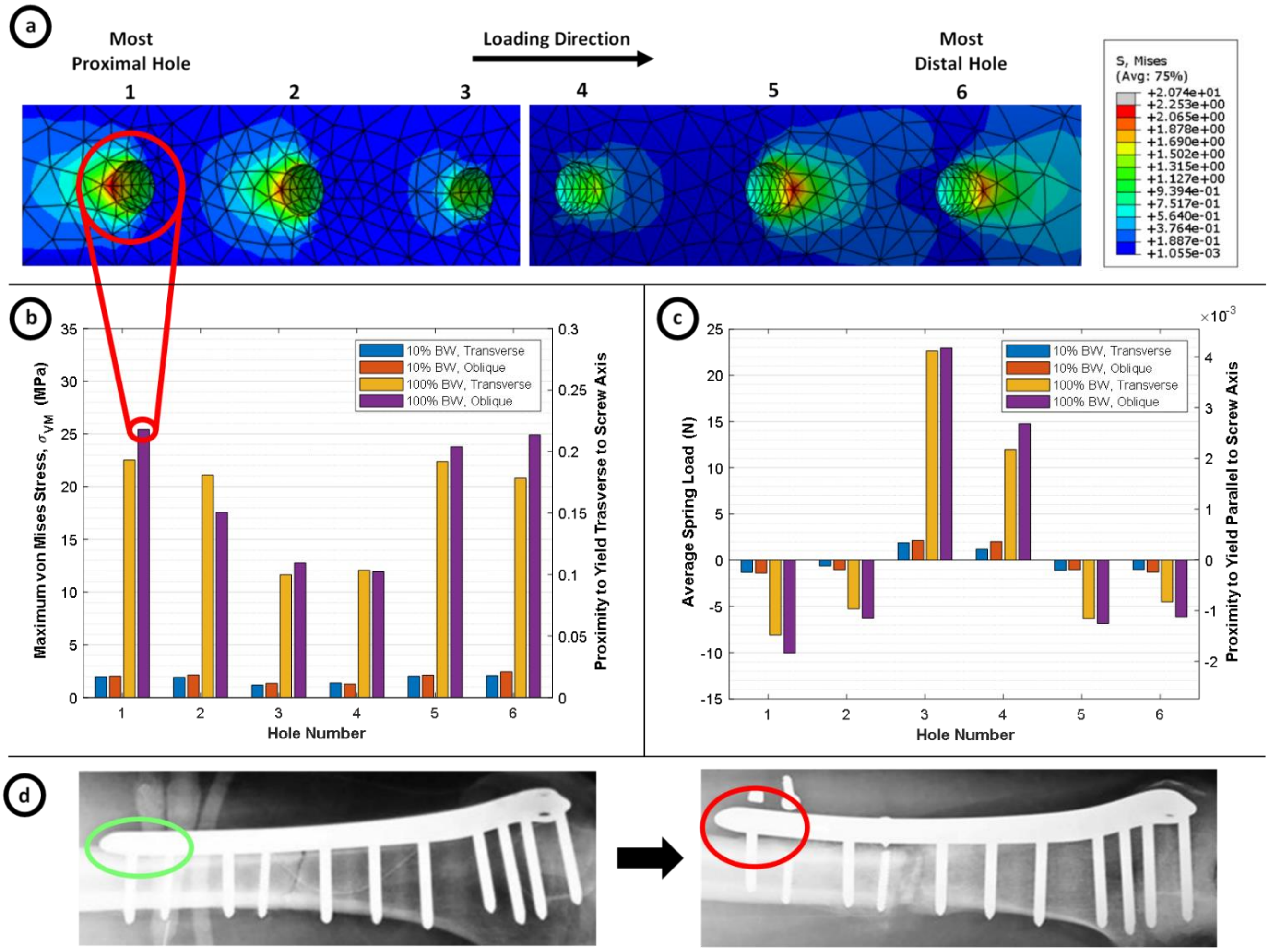

FIGURE 23 | (a) σ_{VM} nephogram (MPa) of the bone for the 100% BW, oblique fracture case; **(b)** σ_{VM_max} in the vicinity of each hole for all investigated permutations of loading and fracture angle; and **(c)** average load within the 8 screw-bone springs at each hole, again, for all investigated permutations of loading and fracture angle (negative values imply screw pull-out, whereas positive values signify screw push-in). Collectively, the data suggests that implant loosening and cut-out is unlikely to occur in a healthy individual who has been correctly operated upon. It also indicates that stress magnitudes within the bone are directly proportional to the magnitude of the applied load and largely insensitive to fracture obliquity. All such findings are as one would intuitively expect [16]. Moreover, since the spring loads are negligible compared to the σ_{VM_max} values, the data indicates that if yielding and loosening were to occur (due to the patient being morbidly obese, for example), the most proximal hole would yield first, in a direction transverse to the screw axis. This is in agreement with **(d)** [60], wherein the maximum deviation of the loosened plate from the bone's surface is seen to be located at its proximal end.

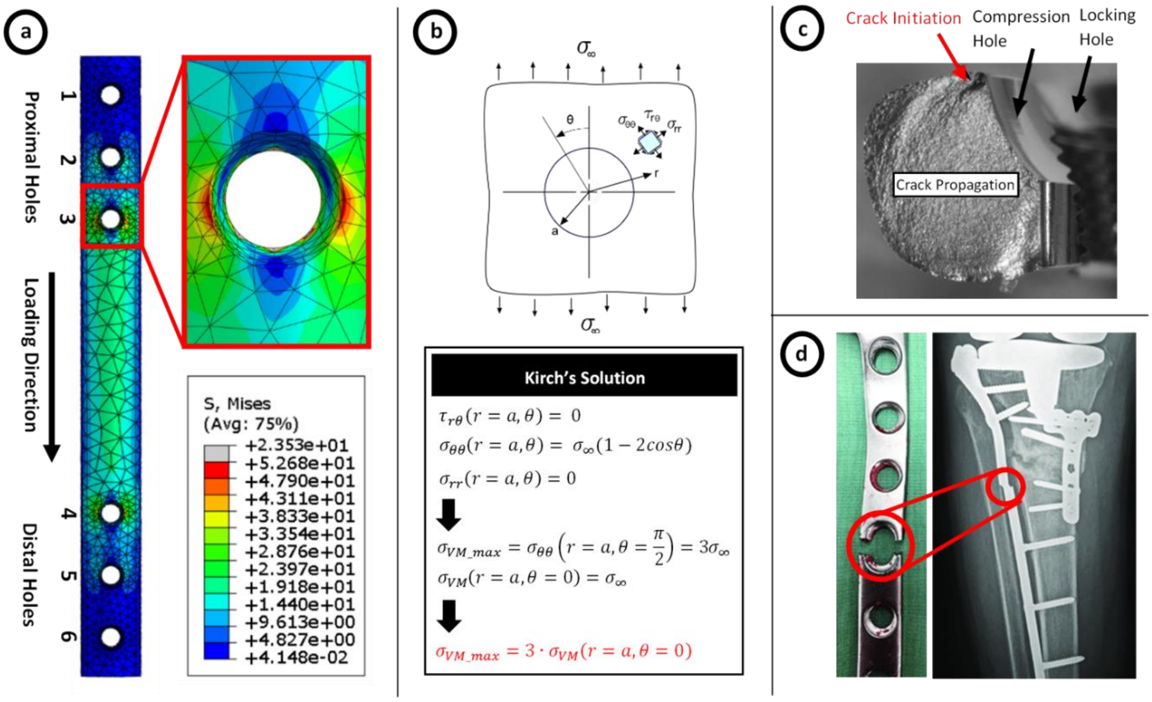

FIGURE 24 | (a) σ_{VM} nephogram (MPa) of the plate for the 100% BW, oblique fracture case. **(b)** This broadly matches Kirch's solution for the stresses at the periphery of a hole embedded within an infinite, two dimensional plate subjected to a uniform, uniaxial remote stress. Additionally, the data is corroborated by various clinical studies that have shown fatigue failure of locked plates initiates **(c)** at the free surface [59], and **(d)** along the periphery of the hole closest to the fracture [59]. Finally, the magnitude of σ_{VM_max} is only a small fraction of the fatigue endurance limit of stainless steel, suggesting fatigue failure during the static weight-bearing phase of recovery rarely occurs in practise. Indeed, this is true [60].

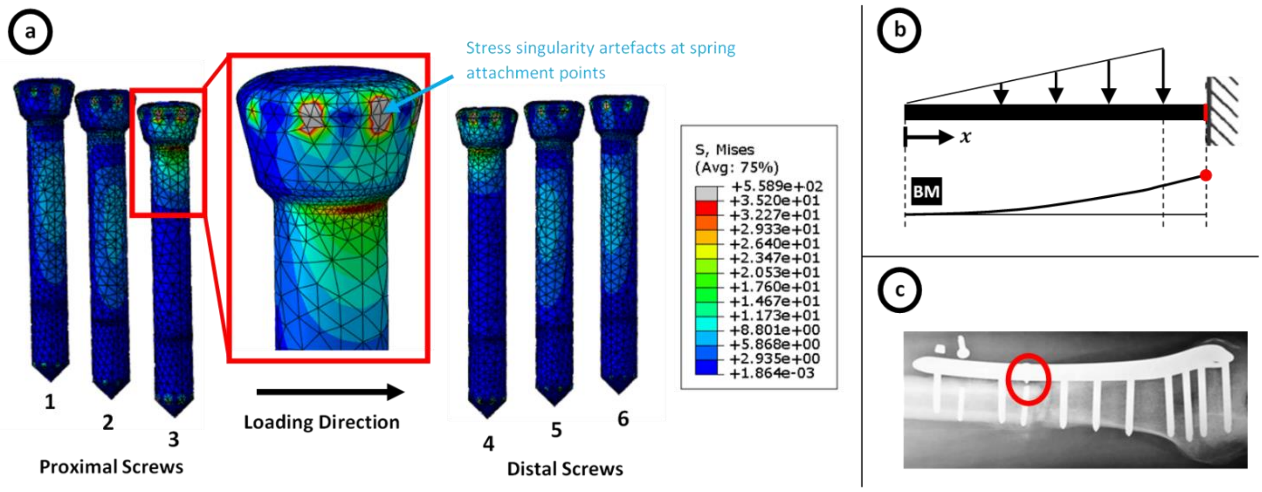

FIGURE 25 | (a) σ_{VM} nephogram (MPa) of the screws for the 100% BW, oblique fracture case, from which it is apparent that σ_{VM_max} occurs at the neck of the screws. **(b)** This coincides with the trivial location of σ_{VM_max} for an analytical model wherein each screw is likened to a built in cantilever beam subjected to a distributed load applied part way along its length. Such a simplification is reasonable as the normal contact stiffness of the screw-plate interface is almost an order of magnitude greater than that of the screw-bone interface. The acquired numerical data is further validated by the radiograph in **(c)** [59], where 3 screws have failed. Of these, it is the most distal screw inserted within the proximal bone fragment that must have been most critically stressed and failed first, since it is the least displaced, which is in turn indicative of a less energetic fracture. As more screws failed, the loads on each of the remaining intact screws would have increased, culminating in more energetic fractures. Similar to the plate, the magnitude of σ_{VM_max} is only very small, suggesting fatigue failure of the screws during the static weight-bearing phase of recovery will rarely occur in practice. Again, this has been shown to be the case [60].

3.4.3 PILOT 3: CONCENTRIC CYLINDERS & IM NAILING

Once a functionally sound model had been developed for the simplistic case of locked plating, the transition to IM nailing was made as a check to ensure the method remained compatible. The soft contact settings defined within the locked plate model were exactly propagated into the present one, before defining 'hard' frictional behaviour at the nail-bone interface. Only springs adjacent to the screw-bone interface were modelled on this occasion, since the holes are not threaded within an IM nail. Furthermore, the total number of springs for each screw was doubled from 8 to 16, to account for the fact that there are now two screw-bone interfaces to be accounted for, either side of the nail. Moreover, to induce bending stresses within the nail and avert trivial, unrealistic uniaxial compression of the assembly, resultant moments and loads, statically equivalent to the action of all tibial muscle forces and knee contact forces listed within TABLE 4, were applied to the most proximal cortical end face of the model [66], [67] (see FIGURE 26).

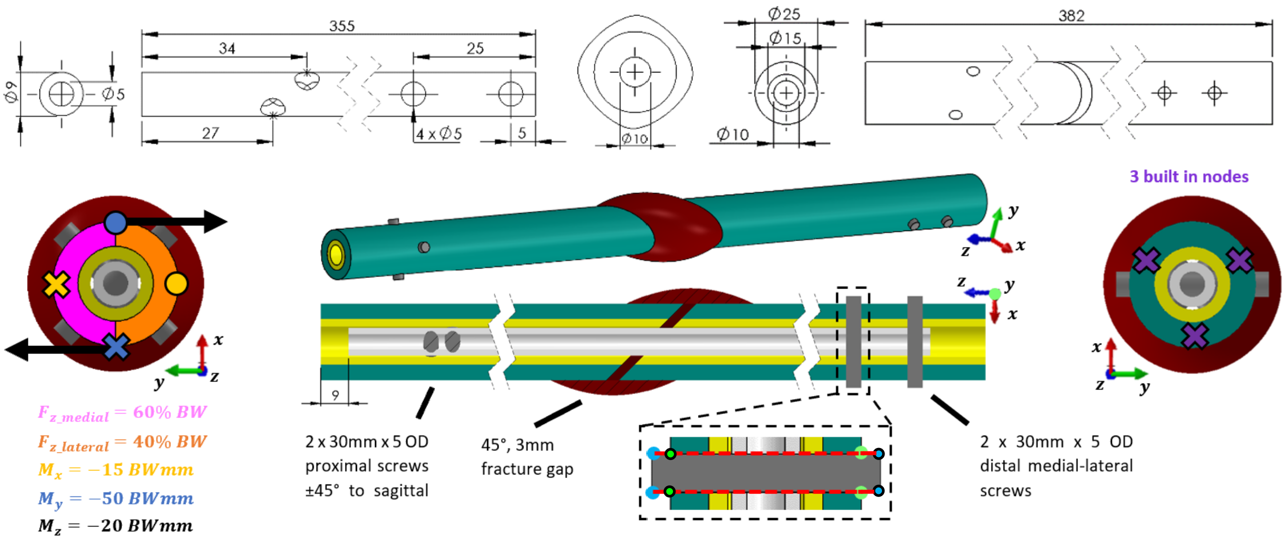

FIGURE 26 | Loads, boundary conditions and important dimensional details of all parts constituting the statically locked and reamed IMN FE model with simplified geometry. The diameter of the reamed hole within the bone is 1 mm greater than that of the 9 mm OD nail, and the geometry of the callus is similar to that defined in FIGURE 8. All loads are applied to the cortical end face of the proximal fragment - the medial and lateral axial loads are uniform pressure loads, whilst ● and ✖ denote moment generating concentrated loads out of and into the page, respectively. For simplicity, all springs at the screw-bone interface extend across the reamed hole – their stiffnesses are as defined in FIGURE 21 and their screw/bone attachment points are represented as ●/● respectively, as well as ●/● respectively.

The model ran satisfactorily with no warnings or error messages, and delivered what may be perceived to be reasonable results. Hence, the novel approach was deemed a great success. Nevertheless, two interesting quirks should be noted.

Firstly, the peak spring load dropped from approximately 23 N to a negligible value of just 5 N at hole 3, as compared to the plating case. This indicates that pull-out/pull-in is not a cause for concern for IMN constructs, and need not be reported amidst the findings of the present study. It also suggests that there is some propensity for removing all springs in their entirety for future analyses, so as to hasten model set-up and processing time. However, this was disregarded following a trial run that terminated unexpectedly in their absence.

Secondly, the much reduced depth of the screw-bone interfaces meant that the stress singularity artefacts arising from the concentrated spring loads began to cloud the stress field within the bone holes to a significant extent, compromising the ability for one to accurately deduce the true stresses in these regions (see FIGURE 26a). In order to circumvent this, it was acknowledged that the contact pressures can be monitored in such locations, as alternative to the von mises stress see FIGURE 26b), since the only information that is lost through making this simplification is that due to axial pull-out/push-in, which has just been proven to be negligible.

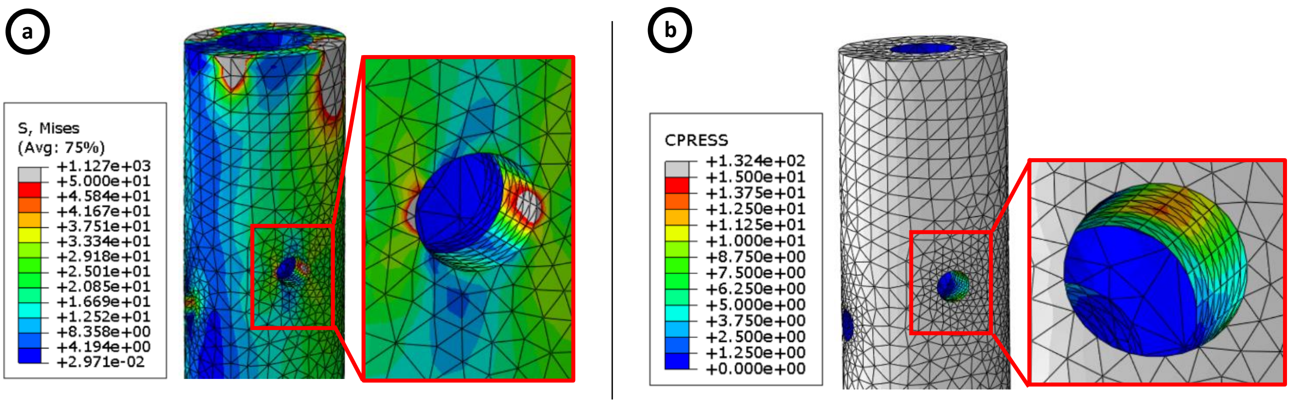

FIGURE 26 | An alternative approach for determining bone stresses in the vicinity of their screw contacts. **(a)** The von Mises stress distribution is markedly clouded by stress singularities at the spring-bone attachment points, giving rise to obscure results, with a notable absence of elevated stresses at the top and bottom of the holes, as one would expect for a predominantly axial loading regime. **(b)** The contact pressure distribution is void of such artefacts, returning results that make far better sense from an engineering perspective.

3.4.4 IMPLICATIONS FOR THE BASE MODEL

Following the promising outcomes of pilot study 3, the novel technique of modelling the screw-bone interface was first propagated across to the base model, with each screw-bone contact being broken down into a softened normal component, as well as an axial component, governed by friction and a set of 8 springs. Hard, frictional contacts were also defined for both the screw-nail and nail-bone interfaces, and the callus was tied to the tibia's periphery, since these were thought to replicate reality exactly.

An initial estimate of the magnitudes of all associated parameters was guided by literature, and is summarised in TABLE 9, overleaf.

TABLE 9 | Initial choice of contact settings for the base model.

Contact Interface	Normal Component	Tangential Component	
		Friction Coefficient	Spring Stiffness
Screw-Bone	Softened, $K_c = 1000\ N/mm$ [61]	$\mu = 0.3$ [68]	$K_S = 785\ N/mm$ [61]
Screw-Nail	Hard [68]	$\mu = 0.3$ [68]	-
Nail-Bone	Hard [68]	$\mu = 0.3$ [68]	-
Callus-Bone	Tied [68]		

3.5 MESHING

IMN FE assemblies are notoriously challenging to process due to their large physical size, need for localized results in various isolated regions, and the substantial amount of contact that must be accounted for during the analyses. Therefore, the establishment of an optimally efficient meshing scheme for all parts was pertinent to the present study so as to maximize the number of parametric studies that could be processed with sufficient accuracy, in a given time frame.

This proved an exigent and laborious task for the tibia in particular, due to its arbitrary morphology. NURBS patches return abhorrent meshes with highly distorted elements that cause an analysis to terminate prematurely. Therefore, these had to be 'erased' using virtual topology and replaced by a new, well-engineered, manually constructed partitioning scheme, which could subsequently be exploited as a means of driving the smallest, computationally demanding elements into only the localized regions in which they were needed (see FIGURE 27a, overleaf). This is in contrast to the other parts, whose uniformly distributed and organized edges granted direct meshing of their imported state.

Previous FE work in this field consistently assigns meshes similar to those outlined in TABLE 8, to IMN assemblies. Hence, these were called upon here for the construction of an initial set of meshes, which would go on to inform a mesh convergence study that is later discussed in section 4 of this report. With all else being equal, the result was an assembly comprising approximately 40% fewer nodes than that delivered by the NURBS patched tibia assembly, and one which returned a far more regulated result (see FIGURE 27b, overleaf), verifying that the tibia had been partitioned sufficiently well.

TABLE 8 | Typical mesh types and sizes reported within literature for IMN FE assemblies. C3D10 and C3D20 elements are of the second order tetrahedral and hexahedral kind, respectively.

Part	Ref.	Element Type	Seed	
			Local	Global
Tibia	[57]	C3D10	1	3.5
Callus	[58]	C3D10		1.5
Nail	[59]	C3D10	1	1.5
Screw	[60]	C3D20R		1

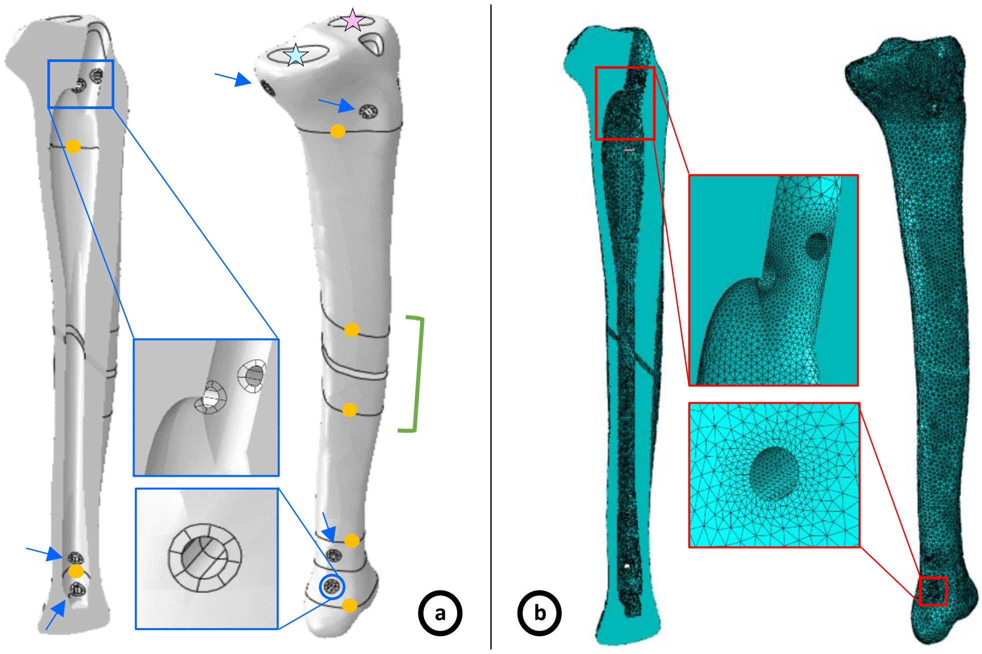

FIGURE 27 | (a) Optimal partitioning scheme for tibia: the dotted partitions regulate a larger global mesh size; the partitions indicated with an arrow ensure a smooth transition to a smaller mesh size and create evenly distributed spring attachment point; and the bracketed region reduces the area over which the bone-callus contact setting must be defined. ☆ and ☆ arise due to the manner in which the knee joint load was applied, as has been discussed previously. **(b)** The resulting mesh, wherein it can be seen that even the most awkward of regions are uniformly meshed to a desired level of refinement.

3.6 OUPUT VARIABLES

As a final step, a MATLAB script of approximately 900 lines was written for the post-processing of a small number of intuitively designed outputs that could be easily interpreted by an orthopaedic surgeon making reference to the results of the parametric analyses. Each falls into one of three main categories, which are sequentially discussed below in the order of their significance.

3.6.1 HEALING PERFORMANCE

Following the decision to model the callus as a single phase part (see section 3.1), deviatoric MR theory (see section 2.3) was called upon as a means of establishing the tissue type and stiffness that each of its constituent elements had the propensity to differentiate into in the next time increment.

The volumes assigned to all elements of callus were first ranked in terms of their associated ε' MR predicted stiffnesses from lowest to highest, prior to performing a cumulative summation of the former. This enabled a cumulative distribution of predicted stiffnesses throughout the callus volume to be subsequently plotted, whose format is extensively described in FIGURE 28, overleaf.

In a bid to further enhance interpretability of the data, all stiffnesses were further normalized by the lower bound stiffness of healed bone, taken here to be that of intermediate bone (1 GPA). This enabled a single, quantifiable *Healing Performance Index* (HPI) to defined as the median normalized stiffness of the callus, facilitating a swift comparison of the susceptibilities of different set-ups to non-union. In other words, a HPI of X means that 50% of the callus has a normalized stiffness of at least X, with $X = 1$ denoting the ideal, fully healed case.

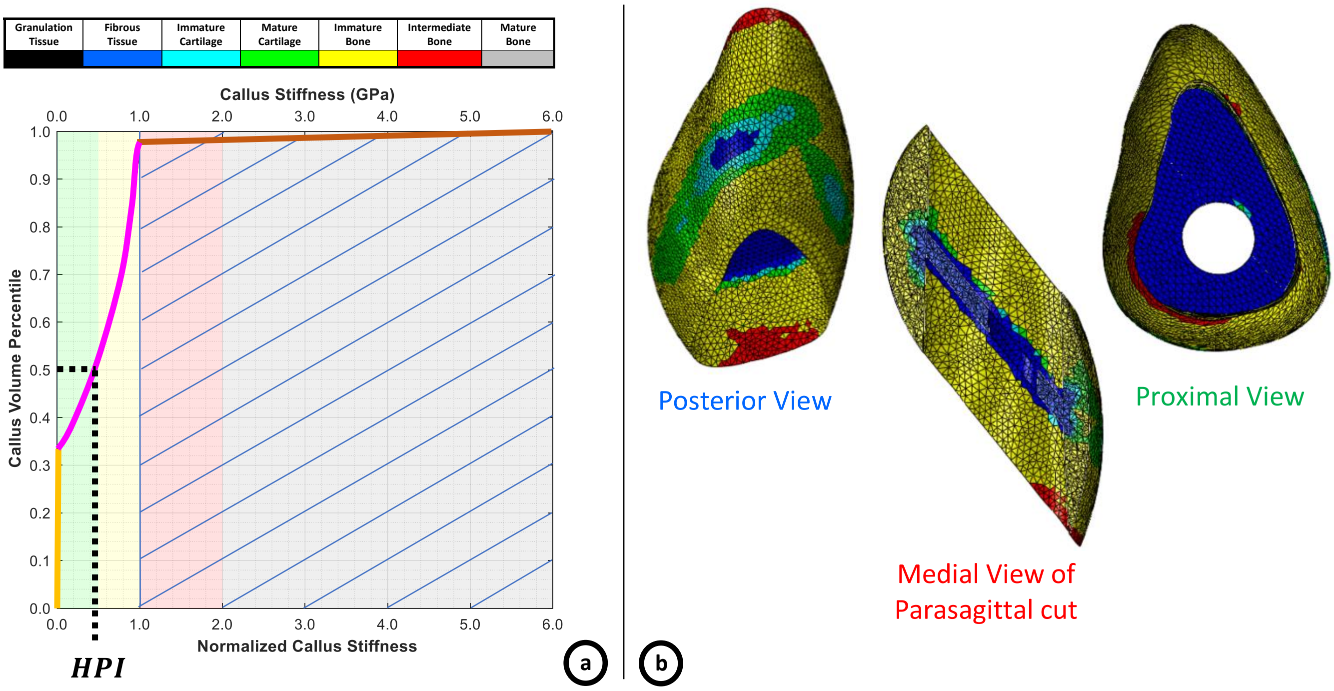

FIGURE 28 | (a) The healing performance plot comprises three distinct regions: the orange portion of the curve accounts for the highly strained, mechanically insensitive granulation and soon to be fibrous tissue that occupies the interfragmentary central portion of the callus; the pink part arises due to large volumes of mechanically sensitive callus being sufficiently stable within the outer portion to differentiate into mature cartilage and immature bone; and finally, the brown section may be attributed to a small number of elements at the callus-bone interface being disposed to little or no strain. The hatched region will be neglected in future plots for the purpose of clarity. **(b)** A pictorial representation may help some readers comprehend the plot's structure more effectively.

3.6.2 INTERFRAGMENTARY MOTION

Whilst the healing performance of a callus can accurately account for the stability of a system and its consequential effect on healing, it cannot be used to delineate the localized loading regime or type of instability that drives non-union. Still, establishing this information may facilitate the design and development of much improved constructs, as well as additional more cost effective revisionary surgery techniques for years to come.

Several surgeons have hypothesized that shear IFM is far more damaging than its axial counterpart. Hence, to make this study more relatable for these personnel, it was decided to study both as part of the parametric analyses, ultimately granting such postulations to be proven or disproven.

This was accomplished by defining six sets of three measurement points on the periphery of the distal fracture face, before projecting these in the axial direction onto the opposing proximal face (see FIGURE 29) and extracting the relative displacement magnitudes of each coupling. Axial IFM was then monitored in the z-direction of the previously discussed global coordinate system of the tibia, whilst shear IFM was evaluated along the fracture face using a newly transformed set of coordinate axes (see FIGURE 29 once more):

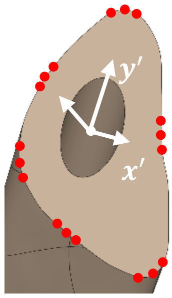

FIGURE 29 | Location of IFM measurement points on the distal fracture face, together with the transformed coordinate axes.

$$IFM_{axial} = |\Delta u_z| \quad (3)$$

$$IFM_{shear} = \sqrt{(\Delta u_x{}')^2 + (\Delta u_y{}')^2} \quad (4)$$

Again to bolster interpretability of the results, a *Shear Index*, SI, was defined as follows:

$$SI = \frac{IFM_{shear}}{IFM_{axial}} \quad (5)$$

A notched box and whisker plot was chosen as the medium through which to present this data, since it grants a prompt assessment of the relative magnitudes of each type of IFM as well as surmises the state of the localized loading regime seen by the fracture (see FIGURE 30).

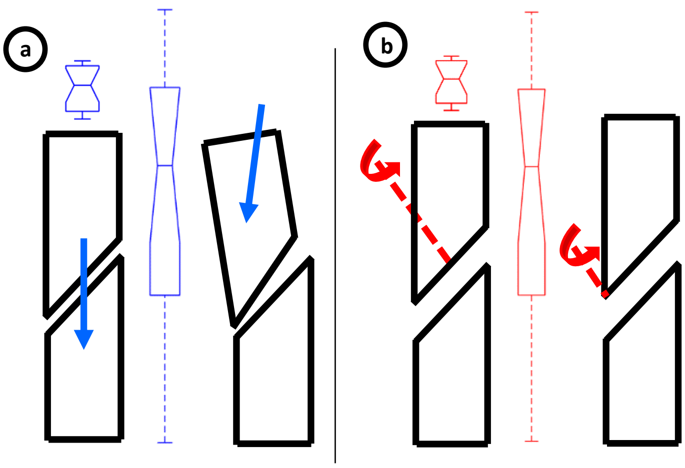

FIGURE 30 | Interpretation of box and whisker plots. (a) A longer axial IFM box translates to more off-axis loading, whilst (b) a longer shear IFM box is representative of torsional rotation about an axis normal to the fracture face, further away from the centroid of the fracture face.

3.6.3 PROXIMITY TO YIELD

Finally, a consideration of the stresses at both the screw-bone and the screw-nail interfaces was deemed necessary to grant a complete description of mechanical performance, as well as an exploration of the principal trade-offs faced by a surgeon tasked with treating LB fractures. Two easy to interpret yielding indices were thus devised.

The first of these was a *Bone Yielding Index* (BYI), taken to be the 95th percentile contact stress (≈ von Mises stress, see section 3.4.3) within a 1mm thick annular ROI that surrounded the most critically stressed bone hole, normalized by the yield strength of bone:

$$BYI = \frac{\sigma_{VM,95,B}}{\sigma_{Y,B}} = \frac{\sigma_{VM,95,B}}{114} \approx \frac{\sigma_{CPESS,95,B}}{114} \quad (6)$$

This convoluted alternative to a simple quotation of the peak stress value was chosen, primarily because it facilitates the acquisition of a fully converged solution, but also because it enables one to establish the bone's proximity to permanently deforming by an amount which may begin to have repercussions for the observed stability of the system in subsequent load cycles.

A *Nail Yielding Index* (NYI) was additionally defined in a similar manner:

$$NYI = \frac{\sigma_{VM,95,N}}{\sigma_{Y,N}} = \frac{\sigma_{VM,95,N}}{860} \quad (7)$$

All screw stresses were dropped from the analyses, since in the absence of threads, these would be so far removed from reality that false conclusions could be drawn.

4 VALIDATION & FINE TUNING

The FE technique is an incredibly powerful methodology for assessing the mechanical performance of a system. However, it can also deliver exceedingly spurious results if a model is set-up incorrectly. This arouses particular cause for concern when analyzing elaborate models, such as an IMN assembly, making their extensive validation an essential part of a given study. Ideally, one would perform an experiment that exactly replicates the FE model, compare results, and subsequently fine tune the model, as a way of mapping the virtualized mechanics to those that are observed in reality. Nevertheless, one does not have this luxury at their disposal during a global pandemic. Hence, the alternative of comparing results to previous experimental studies that are similar to ones FEM, as well as conducting parameter sweeps over all values that all variables that could feasibly take, opting for the one that returns the most sensible solution and noting the potential error associated with such a decision, becomes a necessity. Here, four comprehensive, multi-part investigations were conducted as part of the latter, each of which are presented and briefly discussed in this chapter.

4.1 BONE MORPHOLOGY, MATERIAL PROPERTIES & LOADING

A common approach for validating IMN FE models is to compare the results of a loaded, intact version of the tibia with those reported as part of several older in-vivo and in-vitro experimental studies. A close correspondence then verifies that the reconstruction of the tibia, the assignment of material properties, and the definition of loads have all been done correctly, with sufficient complexity that resembles reality. Typically, a proximal, mid-shaft and distal measurement of bone strain is performed and compared to the findings of [69], [70], and [71], respectively. These are summarized in TABLE 9, below.

TABLE 9 | Summary of the intact tibia experimental studies used for validation purposes in this work.

ROI	Ref.	Type	Description	Compressive Strain		Tensile Strain	
				Magnitude (με)	Location	Magnitude (με)	Location
Proximal	[69]	In-vitro	Single leg stance of 21 year old female, two pint evenly distributed load of 50 kg.	220	Posterior surface, 75 mm below the tibial plateau	125	Lateral surface, 25 mm below the tibial plateau
Mid-Shaft	[70]	In-vivo	Normal walking using a Dynamic Gait Simulator (DGS).	230	Medial surface		
Distal	[71]	In-vivo	35 year old, 1.7 m tall, 68 kg male at 45% Gait.	1431±310	Posterior surface, 90 mm above malleoli	719±469	Anterior border, 90 mm above malleoli

In light of the above, appropriate modifications were first made to the base model for its validation against these studies. This saw the knee joint loads ramped up to 100% bodyweight in every case, whilst for [69], the ankle joint reaction forces and muscle forces had to further be removed from the Sawbones tibia, whose distal epiphysis was then assigned the 'encastre' boundary condition (see FIGURE 31). The resulting set-ups returned the following outputs, which have been provided in the context of those of two other state-of-the-art FE studies to aid a more thorough evaluation of validity:

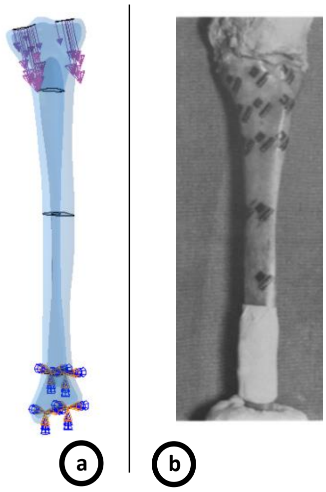

FIGURE 31 | (a) Intact tibia FE model with simplified loading, and **(b)** the experimental set-up it sought to replicate.

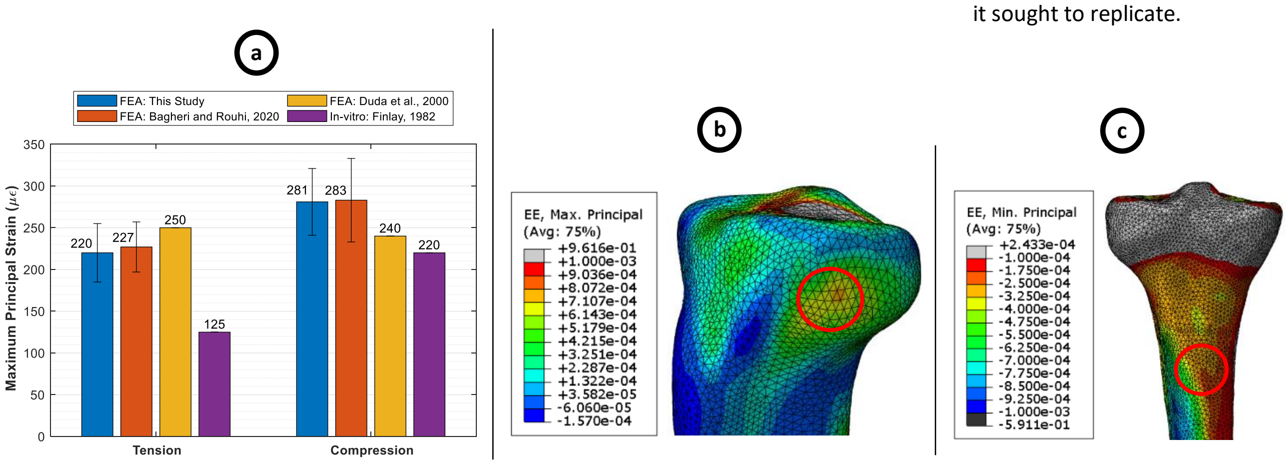

FIGURE 32 | Proximal measurement of intact tibia validation results. **(a)** A comparison of the strain magnitudes with the outputs of other studies. These are all of similar size with the exception of the anomalous experimental tensile strain. **(b)** and **(c)** highlight the probed regions on the lateral and posterior surfaces, respectively, used to acquire the tensile and compressive strain magnitudes, respectively, for this study.

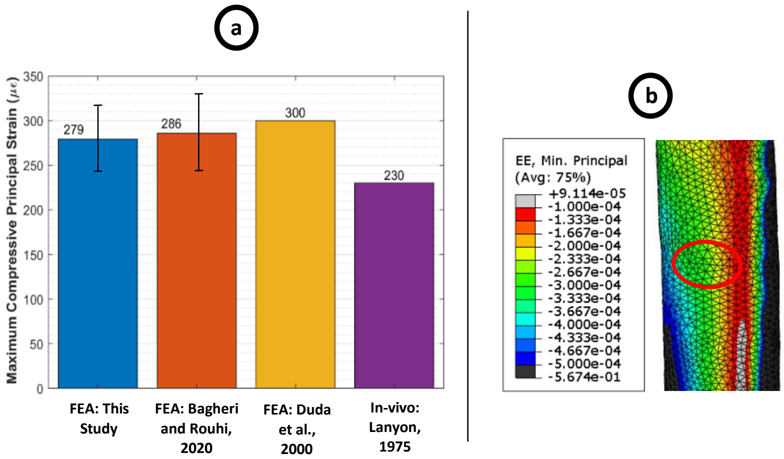

FIGURE 33 | Mid-shaft measurement of intact tibia validation results. **(a)** A comparison of the strain magnitudes with the outputs of other studies. Again, these are all of similar size with a smaller result being seen for the experimental study as compared to the FE analyses. **(b)** highlights the probed region on the medial surface used to acquire the compressive strain magnitude for this study.

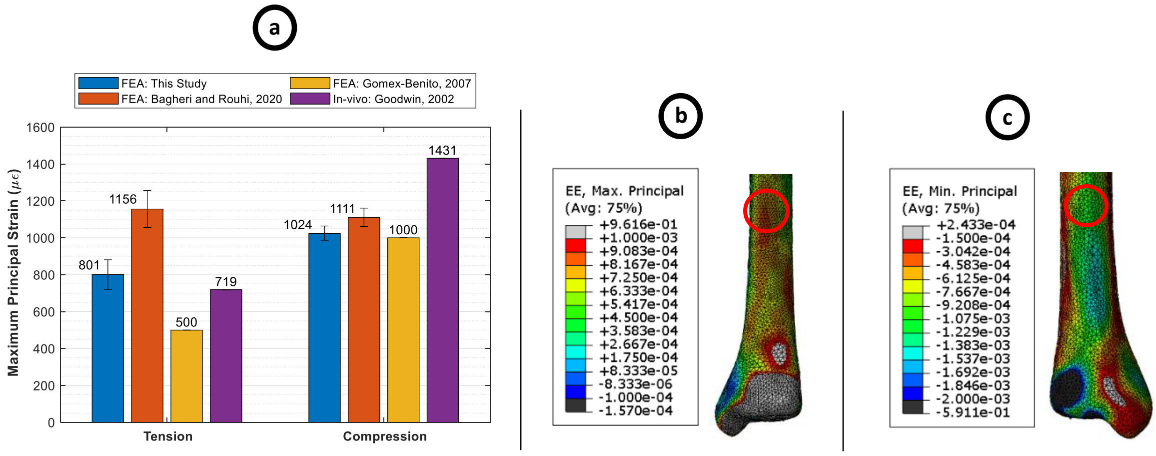

FIGURE 34 | Distal measurement of intact tibia validation results. **(a)** A comparison of the strain magnitudes with the outputs of other studies. There is some considerable degree of variation amongst the tensional results, yet this study returned a magnitude for this variable very similar in size to that which was experimentally acquired. **(b)** and **(c)** highlight the probed regions on the anterior border and posterior surface used to determine the tensile and compressive strain magnitudes for this study.

It can be observed from FIGURES 32, 33 and 34, alike that the results from the FE studies are consistently similar to one another, although these can differ quite markedly from their respective experimental values. In general, such discrepancies are far vaster in the proximal and distal measurement locations, as compared to the mid-shaft. Hence, one can quite confidently discern that their causes are not due to overly poor experimental practise, rather the simplified, artificial fixation and loading regimes that must be imposed upon the virtual tibia as part of the FE method, if results are to be acquired in a reasonable time frame. That said, the strain gauges can have a marginal reinforcing effect upon the medium they are adhered to, hence, although only slight, this would also contribute to the much reduced strain values that were observed experimentally.

Saint-Venant's principle tells us that the exact distribution of a load is not important far away from the loaded region, as long as the resultants of the load are correct. Therefore, since the lower bound compressive mid-shaft strain that was probed in this study (239 με) falls within 3.9% of that which was derived by [70] experimentally, and because an assessment of the mechanical performance of the fracture site falls at the heart of this study, the morphology of the Sawbones tibia, its anisotropic material properties, and the physiological loads that were defined upon it, were, here, all considered valid, and it was accepted that bone stresses may be underpredicted to some extent.

Following this conclusion, a swift test was run to elucidate the computational savings associated with enforcing isotropic as opposed to anisotropic material properties for the bone. A total saving of just 4.8 % was discovered, which is in close agreement with what was read in literature. Hence, the anisotropic formulation was retained in the base model.

4.2 CALLUS MATERIAL PROPERTIES

TABLE 9 | Bi-phasic, poroelastic material properties of granulation tissue.

Young's modulus	0.2	MPa
Permeability	1e-14	m^4/Ns
Poisson's ratio	0.167	
Solid Bulk modulus	2300	MPa
Fluid bulk modulus	2300	MPa
Porosity	0.8	

An accurate determination of the healing performance of LB fractures underpins the findings of this study. Therefore, the callus and tibia of the base model were meshed using poroelastic C3D8RP elements, the material properties of the callus were modified to be bi-phasic (see TABLE 10) and a poroelastic analysis was run in Soil step of ABAQUS to unequivocally establish whether bi-phasic simulations, together with a bi-phasic MR data processing technique would provide benefits over the single phase ε' regulated base model for the parametric studies. Both pictorial representations of the callus and its healing performance plot were critically assessed and compared to those of the base model so as to inform this subjective decision (see FIGURES 35 and 36, respectively).

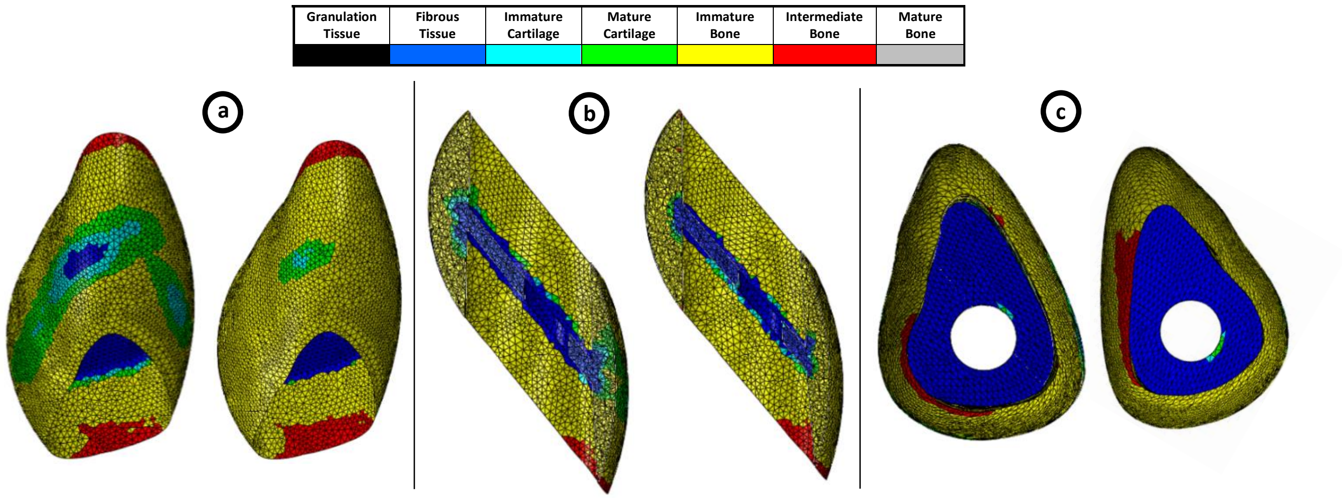

FIGURE 35 | Visual side-by-side comparison of the tissue types that a callus of granulation tissue has some propensity to differentiate into in the next time increment. Images on the left hand side of each pair are taken from the single phase base model, whereas those on the right relate to the bi-phasic alternative. **(a)** Anterior view; **(b)** Medial view of parasagittal cross section; and **(c)** Proximal view, normal to the fracture plane.

The outputted data proved convincing. It was found that a single phase callus post processed using $\boldsymbol{\varepsilon}'$ theory returns a HPI that is 6.4% smaller than that of its superior bi-phasic alternative, with the central portion of callus being the most drastically influenced. Conceptually this makes sense, since it is only fluid flow velocity that tells the two models apart, and it is this that changes most rapidly in the central region when disposed to loading.

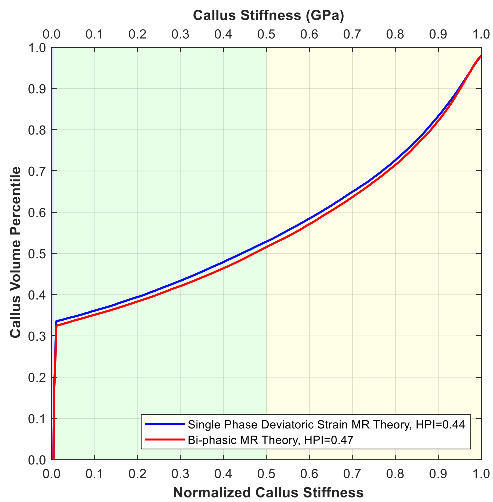

FIGURE 36 | Healing performance plot demonstrating a negligible difference between the single phase and bi-phasic models.

In terms of computation time, the base model ran approximately 10 times faster than the bi-phasic case, which took an astonishing 80 hours to process using 48 cores on Imperial's High Performance Computing Service (HPC). Hence, the author was left little choice but to continue pursuing the more elementary, single phase scenario.

4.3 CONTACT SETTINGS

Section 3.4 outlined a novel approach for modelling the screw-bone interface, which sees the standard tie contacts reported in literature, substituted by a frictional, softened normal contact, as well as a set of 8 springs that each run axially along the periphery of the screw in question. It was also demonstrated how tuning the settings of these parameters would prove pertinent should one wish to fully and accurately characterise the healing potential of a callus.

Numerous attempts were made to do this through the use of experimental data reported amid literature (see FIGURE 37a). However, the method was dismally unsuccessful since the author could not establish the exact manner in which the bone is fixated nor loaded in any case. Consequently, a localised sub model of the threaded screw bone interface, at what was known to be the most critically stressed region of the assembly, was created as an alternative medium through which these parameters could be determined (see FIGURE 37b).

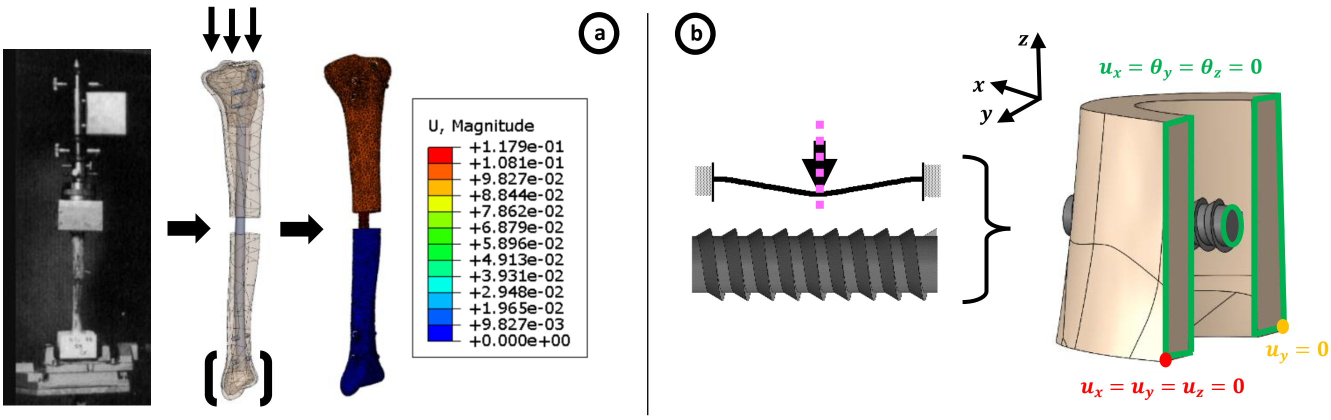

FIGURE 37 | Tuning contact settings. **(a)** The experimental method of [69] was replicated in virtual space, with the distal epiphysis built in and a uniformly distributed load applied to the proximal epiphysis. The overall compliance of the assembly was then determined using the FE method, but the output was 10 x too stiff. **(b)** The alternative approach of sub modelling the medial portion of hole 4 was instead adopted. Since each IMN screw may be approximated as a symmetrically loaded, built in bridging beam, the problem size may be reduced by exploiting approximate planes of symmetry.

The full dimensional details of the Stryker screw that was modelled are given in TABLE 10, opposite.

First a virtual pull-out test was conducted, wherein a representative distributed load was applied in

TABLE 10 | Design parameters for the Stryker 1896-50505 screw.

	Variable	Symbol	Value	Unit
Screw	Outer Diameter	D	5	mm
	Core Diameter	d	3.9	mm
	Pitch	P	1.75	mm
	Pilot Hole Diameter	h	4.1	mm

the axial direction of the screw, and its resulting axial displacement was monitored. The screw was displaced by 0.0637 mm under an axial load of 100 N, hence the required stiffness of each of the eight springs within the base model per screw-bone contact in the base model was deemed to be 393 N/mm – a result that deviates by just 4.3% from that which may be computed from the axial pull out test results of [72] for a 5mm locking screw inserted within a femoral diaphysis. Thus, the sub model was perceived to be valid and could be used with confidence for establishing a reasonable value for the softened normal contact stiffnesses.

This time, a representative load of 239 N was applied to the screw's end in the normal direction and the resulting displacement magnitude of 0.443 mm was noted as a datum for the simplified plain cylinder model. Where appropriate, this was made to entirely equivalent to that given in FIGURE 37b and the newly established spring stiffnesses were defined. The normal contact formulation was then varied as part of a series of iterative analyses, whose results are given in TABLE 11, opposite, and from which the linear formulation of 1000 N/mm that was originally assigned to the base model was concluded optimal. This is because whilst the 500 N/mm case returned the smallest percentage error in terms of compliance, its associated stress field was so suppressed that it may not have deviated significantly from case to case as part of the parametric analyses, thus rendering BYI computations useless. In a bid to compensate for the artificial relaxation of stress observed for the for the chosen formulation, pairs of screw-bone and cylinder-bone sub-model analyses were run side by side for incrementing values of applied load, before generating a stress mapping function, which was to be used for a more realistic computation of BYIs (see FIGURE 38).

TABLE 11 | Normal contact stiffness tuning results, wherein the target datum is highlighted in green, and the selected formulation is given in red

Formulation	Δu (mm)	% Error
Threaded	0.443	0.0
Hard	0.211	-52.4
Tied	0.202	-54.4
2000 N/mm	0.417	-5.9
1500 N/mm	0.423	-4.5
1000 N/mm	0.427	-3.6
500 N/mm	0.432	-2.5

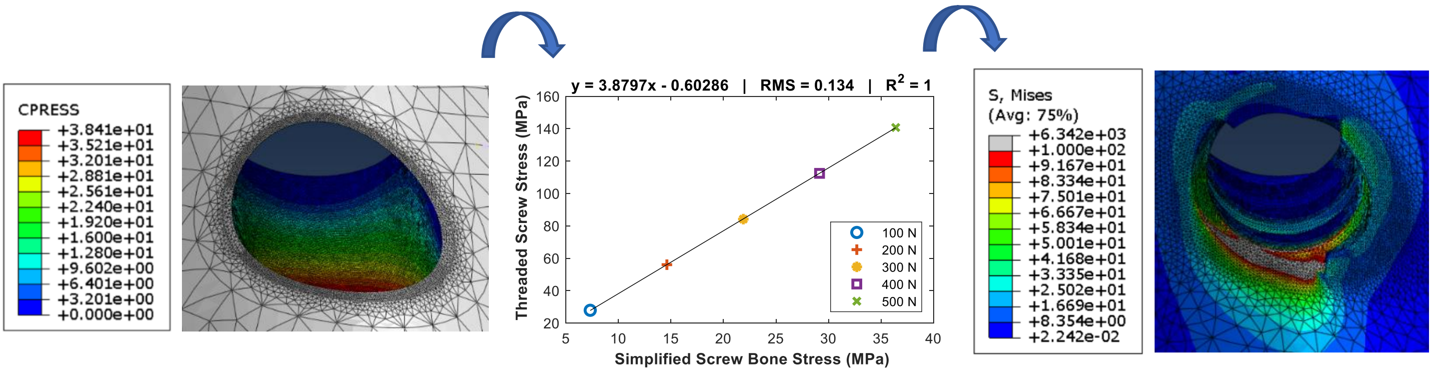

FIGURE 38 | Stress mapping function for translating the stresses seen at the bone-cylinder interface to those that actually occur at the screw-bone interface. 95th percentiles of stress were used in all cases.

This mapping technique was similarly implemented for the screw nail-interface (see FIGURE 39), since whilst this was to be treated as a hard rather than soft interface, the stress concentrating effects of the screw threads upon the nail's surface ought still to be allowed for in the evaluation of the NYIs.

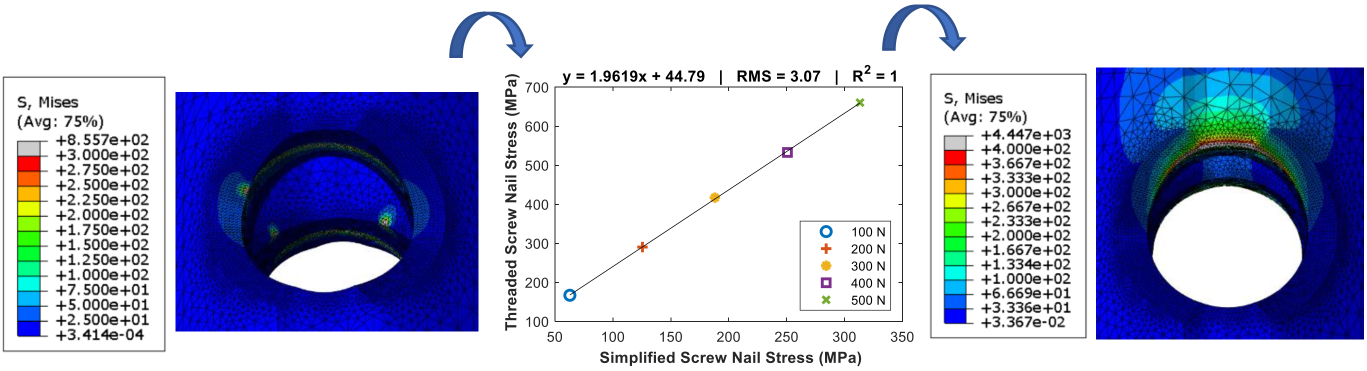

FIGURE 39 | Stress mapping function for translating the stresses seen at the nail-cylinder interface to those that actually occur at the screw-nail interface. 95th percentiles of stress were used in all cases.

Finally, once the above interfaces had been carefully characterized, a move was made away from the localized region of the sub-model and an exhaustive sensitivity study was conducted for all contact settings that constituted the base model as a whole. The consequential effects of halving and doubling the magnitude of each setting were monitored, giving the data that is concisely reported in TABLE 12, below.

TABLE 12 | Contact setting sensitivity study results. All setting adjustments that gave rise to a change from the base model of greater than 5% are highlighted in yellow, whilst the percentage differences that reinforce the hypothesis that other models in this field are inaccurate due to their adoption of tied contacts, are highlighted in orange.

			Base Model	Sensitivity Study						
				Friction Coefficient		Spring Stiffness		Normal Contact Stiffness		Tied Contacts
Contact Settings	μ	-	0.3	0.15	0.6	0.3	0.3	0.3	0.3	-
	k_s	N/mm	389	389	389	195	778	389	389	
	k_c	N/mm	1000	1000	1000	1000	1000	500	2000	
IFM	Axial	mm	0.332	0.338	0.327	0.333	0.331	0.336	0.323	0.098
				+1.81%	*-1.46%*	*+0.30%*	*-0.30%*	*+1.17%*	*-2.71%*	*-70.48%*
	Shear	mm	0.718	0.718	0.694	0.721	0.716	0.719	0.717	0.856
				0.00%	*-3.34%*	*+0.04%*	*-0.03%*	*+0.17%*	*-0.14%*	*-16.12%*
HPI			0.44	0.43	0.43	0.43	0.44	0.45	0.45	0.17
				-2.3%	*+1.3%*	*-2.3%*	*0.0%*	*+2.3%*	*+2.3%*	*-61.4%*
NYI			0.66	0.73	0.58	0.66	0.66	0.68	0.64	0.52
				+10.6%	*-13.3%*	*0.0%*	*0.0%*	*+3.0%*	*-3.0%*	*-21.2%*
BYI			0.80	0.85	0.77	0.77	0.79	0.51	1.70	0.658
				+6.3%	*-3.8%*	*-3.8%*	*-1.3%*	*-36.3%*	*+112.5%*	*-17.8%*

Most crucially, the findings demonstrate that none of the contact settings have a significant effect on the evaluation of the healing performance and stability of a set-up, yet tied contacts can artificially instill up to a 70% elevation in fracture stability. Moreover, it can be seen that ties markedly diminish stress magnitudes at the screw-bone and screw-nail interfaces. These two factors in tandem emphasize the uniqueness of the present study in terms of how it will be the first of its kind to accurately establish the mechanical response of a set-up.

Other than the tied contacts, there are four deviations that fall beyond the 5% threshold, yet these are not strictly significant as they could be compensated for in a new computation of the stress mappings.

4.4 MESH CONVERGENCE

Once all parts of the model had been validated and all fine tuning was complete, a mesh convergence study could finally be conducted to establish the minimum number of elements required for a sufficiently accurate solution. This task was split into two principal stages. First, the callus was iteratively re-meshed with global seeds of 2.5 mm, 2 mm, 1.5 mm and 1mm, giving the healing performance convergence plot in FIGURE 40, below. Then, the local hole seed of the tibia and nail, as well as the global seed of the screws, were each modified to 1.5 mm, 1 mm, 0.75 mm and 0.5 mm, and the resulting BYIs and NYIs were monitored, giving the second mesh convergence plot seen in FIGURE 41, opposite.

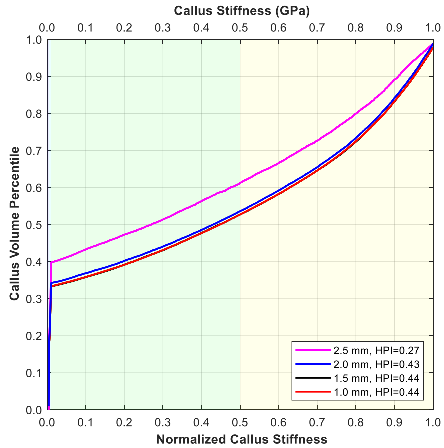

FIGURE 40 | Healing performance mesh convergence plot for the callus .

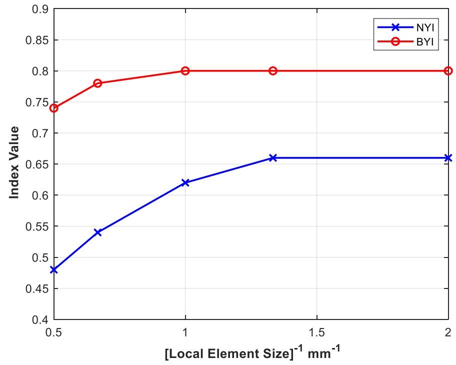

FIGURE 41 | NYI and BYI mesh convergence plots for the bone and nail holes, as well as screws.

It can be seen that in the case of the callus, a fully converged solution, taken here as a less than 5% error, was achieved with a 1.5 mm mesh, whilst a far more refined mesh size of 0.75 mm was required to achieve the same accuracy in the other regions.

A full breakdown of the base model's mesh following the assignment of these new seed sizes is given in TABLE 13, below.

TABLE 13 | Breakdown of the base model's final mesh.

Part	Element Type	Local Seed	Global seed	No. of Elements	No. of Nodes
Tibia	C3D10	0.75	3.5	407,920	591,486
Callus	C3D10		1.5	68,278	104,722
Nail	C3D10	0.75	1.5	54,085	90,410
Screws (x4, total)	C6D20R		0.75	1,8362	84,769
Assembly				548,645	871,414

5 PARAMETRIC STUDIES

This final chapter of this report will provide a succinct description and interpretation of the results acquired for each of the parametric studies. Furthermore, since conducting a complete parameter sweep of all variables associated with IMN fixated LB fractures is very nearly an impossible task, justifications for the small number of the parameters that were investigated will also be presented. All models were constructed using the same modelling framework as has been extensively addressed in chapters 3 and 4 of this report.

5.1 FRACTURE GEOMETRY

45ML-45AP fractures are by far the most prevalent LB fracture type that is observed clinically. Consequently, surgeons currently grow increasingly uncertain as to how to treat a given fracture the more its geometry deviates from this standard case. This study thus sought to elucidate the effects that fracture gap size, degree of obliquity and plane of obliquity have on a given assembly's performance. Fracture gap sizes of 2, 3 and 4 mm, as well as fracture angles termed 20ML-45AP, 45ML-20AP, 45ML-45AP, 70ML-45AP and 45ML-70AP were therefore all analyzed.

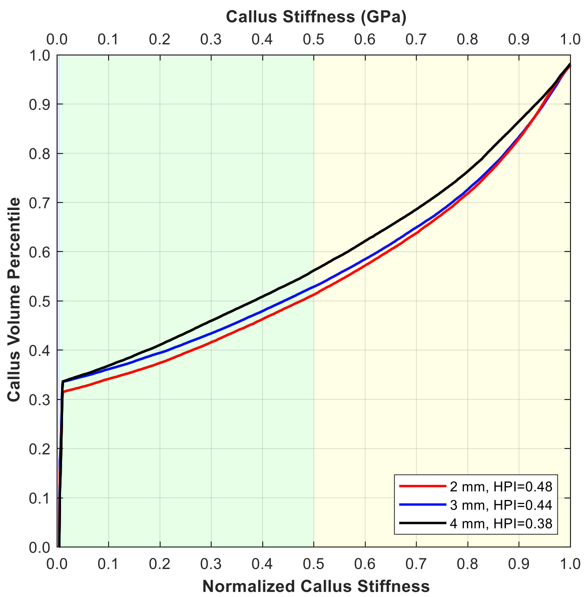

FIGURE 42 | Healing performance plot for different fracture gap sizes.

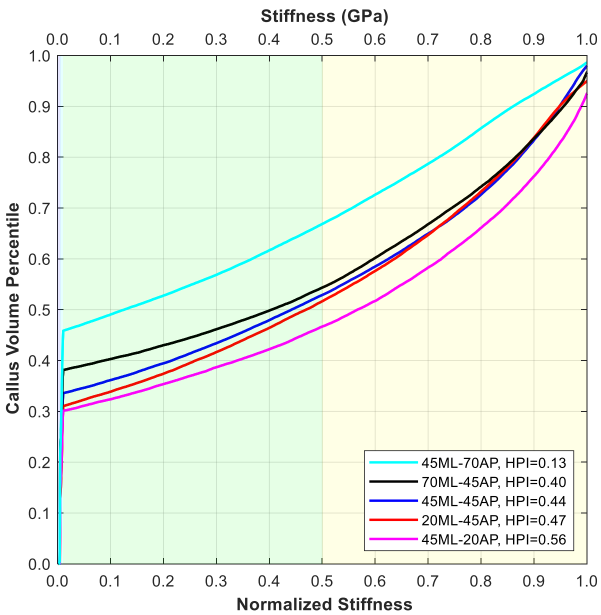

FIGURE 43 | Healing performance plot for fractures of differing degrees and planes of obliquity.

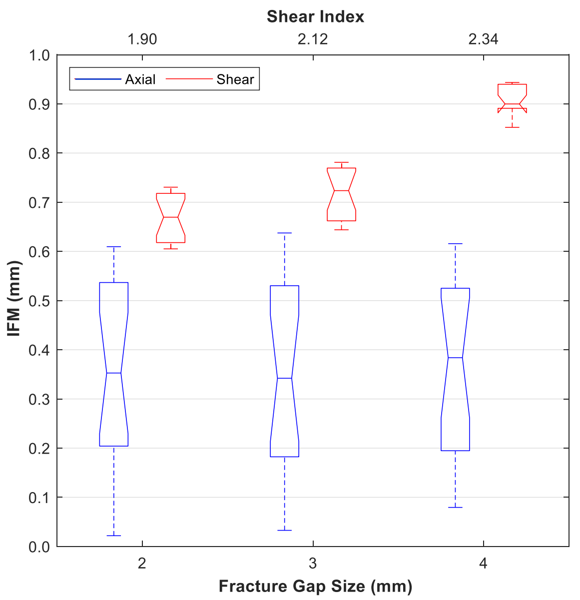

FIGURE 44 | Axial and shear IFMs for different fracture gap sizes.

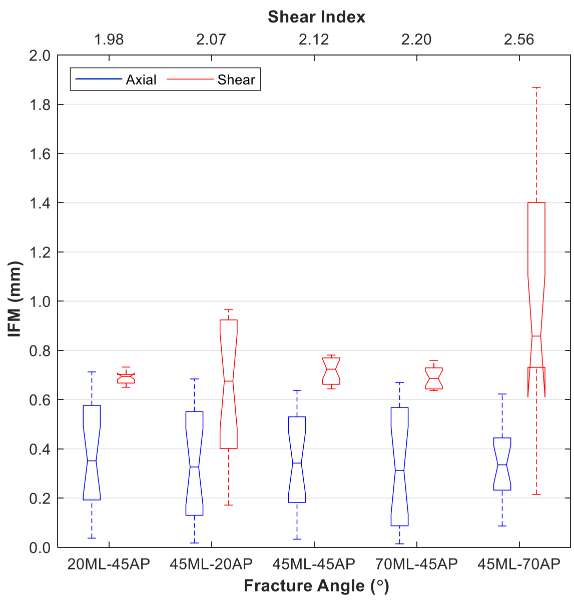

FIGURE 45 | Axial and shear IFMs for fractures of differing degrees and planes of obliquity.

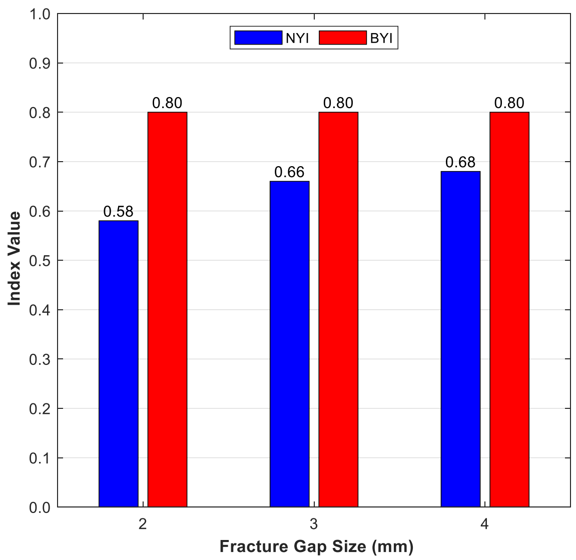

FIGURE 46 | NYIs and BYIs for different fracture gap sizes.

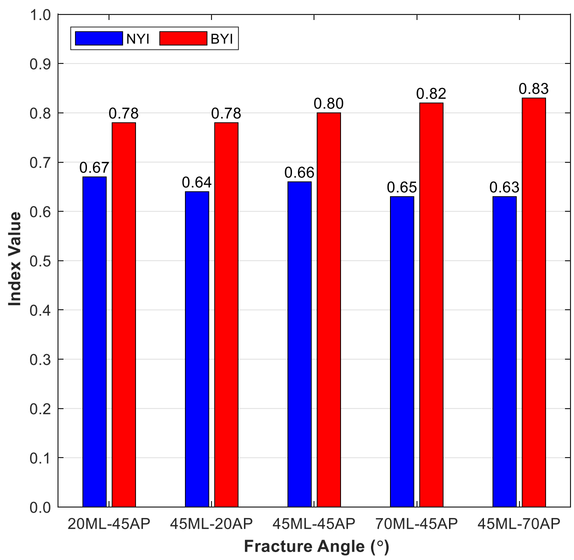

FIGURE 47 | NYIs and BYIs for fractures of differing degrees and planes of obliquity.

It is apparent from the figures that larger fracture gap sizes will return inferior healing performances, which in general holds true for any type of fracture in any bone of the body. This can be attributed to a larger proportion of the callus being situated in the central, interfragmentary region, which itself is disposed to greater mechanical stimuli than the periphery. Still, this relationship is not linear, with the 2mm and 3mm gaps returning very similar HPIs, yet both being substantially larger than that of the 4mm case. As such, whilst a good reduction of a fracture is important for revascularization and healing, the benefits of say a reduction from 3 to 2 mm may be overridden by the compromise in vascularity that is caused by the extra manipulation of the bone fragments that is necessary to achieve such a reduction. Therefore, it appears as though a 3mm fracture gap may achieve the best compromise.

It can also be seen that fractures of greater obliquity are more susceptible to non-union and that having this obliquity in the AP rather than ML direction further amplifies this. This is because fracture faces in the AP direction have a greater surface area, thus a larger proportion of the callus is again found within the critically strained interfragmentary zone.

Furthermore, the strong correlation between shear index and healing performance should be noted - larger fracture gaps that are of greater obliquity and which are tending towards the AP direction mean that a larger component of the knee contact load acts along the fracture plane, promoting more shear IFM and thus heightening the magnitude of deviatoric strain stimuli seen by the callus.

5.2 PRIMARY INTERVENTION STRATEGY

Stryker list nails of 9 mm diameter through to 15 mm diameter in 1 mm increments within their 'Standard T2 Tibia' catalogue. They claim that the 10 mm version suffices for most individuals, yet they do not offer any suggestions as to when an alternative size may be required. Hence, the first part of this second parametric study sought to establish this information by analyzing the performance of a 9 mm, 10 mm, 11 mm and 12 mm nail. Larger nails could not be investigated since these were incompatible with the Sawbones tibia, giving too little an edge margin between the endosteum and periosteum layers.

Different screw configurations also received some attention. Stryker declare that hole positions 12-45 must always be occupied, yet there is some propensity for incorporating an additional 5th screw either proximally , or distally. The use of all 6 screws may also be an option. Hence, this study further sought to demystify the air of confusion that surrounds this selection by comparing the mechanical response of configurations 12-34, 123-4, 12-34 and 123-456 simultaneously.

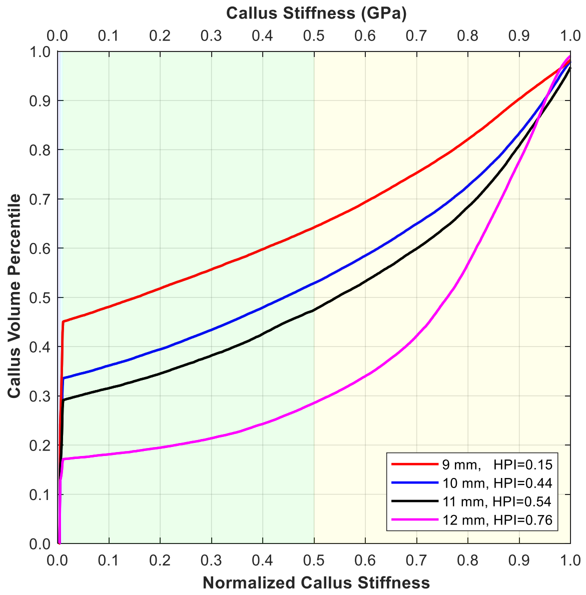

FIGURE 48 | Healing performance plot for nails of different diameters.

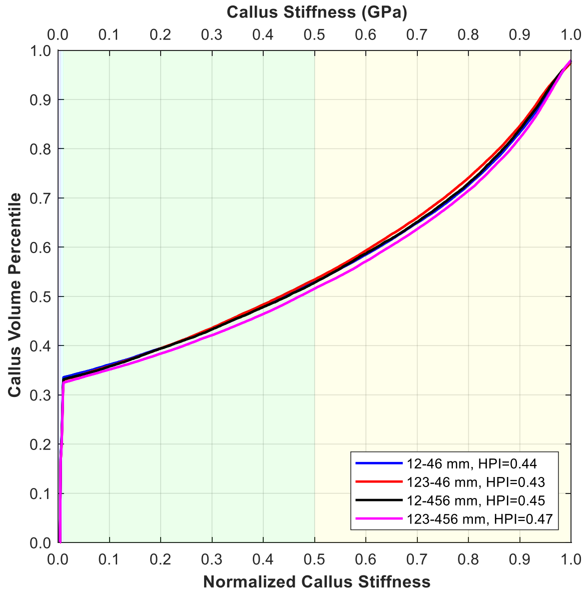

FIGURE 49 | Healing performance plot for different screw configuration patterns.

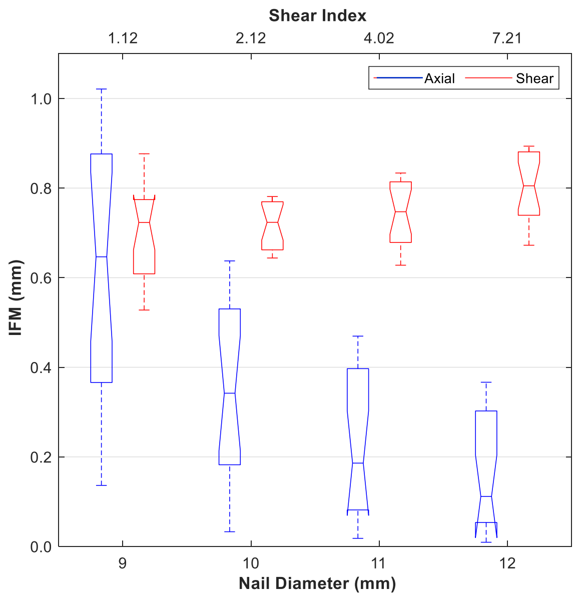

FIGURE 50 | Axial and shear IFMs for different nail diameters.

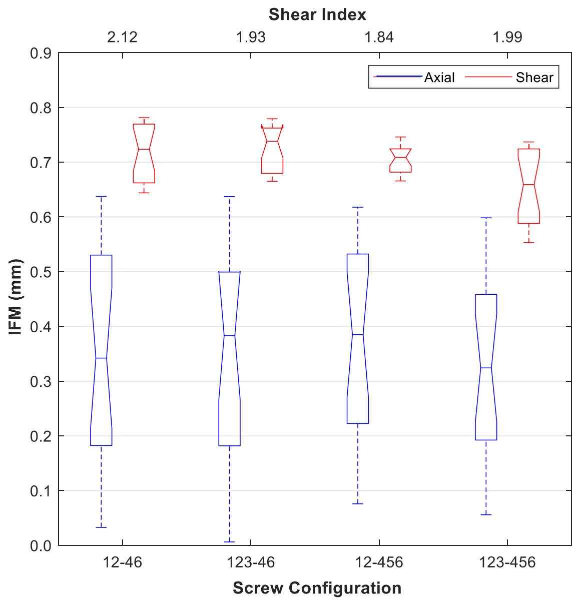

FIGURE 51 | Axial and shear IFMs for different screw configurations.

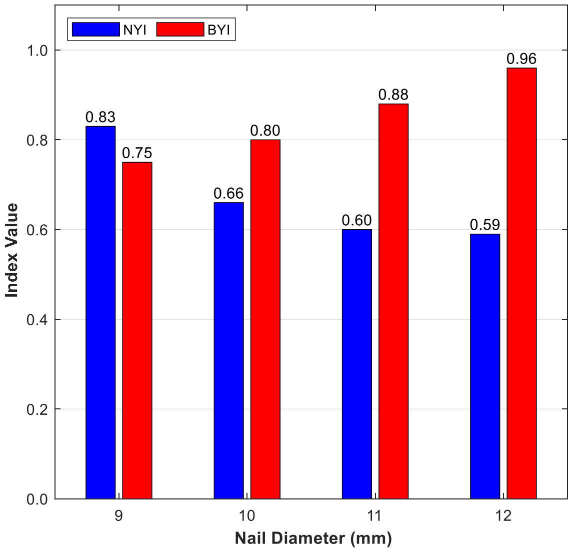

FIGURE 52 | NYIs and BYIs for different nail diameters.

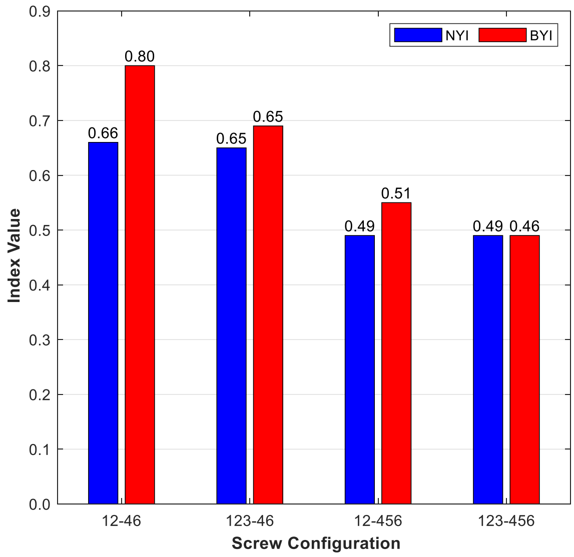

FIGURE 53 | NYIs and BYIs for screw configurations.

The most significant finding here is that a marginal increase in nail diameter can culminate in a mammoth rise in axial structural stability, which is as expected given that the flexural rigidity of a cylindrical rod scales as D^4. However, more obscurely, this is accompanied by a slight rise in shear IFM. Such a peculiarity can be explained by the fact that when a nail is loaded, it becomes slightly cambered, before making contact with the reamed surface at the mid-shaft location. As the nail's stiffness increases, its camber becomes smaller, and thus it imparts a reduced normal contact force upon the bone's inner surface, curtailing the stabilizing frictional loads in the tangential directions also. Interestingly, this entirely contradicts the hypothesized theories that it is the SI that dictates the healing pathway of a fracture. Hence, it can be concluded that bone tissue is more sensitive to shear stimuli than axial stimuli, but since this difference is slight, it can be become masked if the magnitudes of the axial stimuli are far vaster than those in shear.

A further unusual finding is that the screw configuration has next to little effect on IFM and thus healing performance. This is in stark contrast to other work in this field that has reported a general incline in in stiffness the more screws that are added. However, the author is obliged to believe that that their work is inaccurate due to their prevalent use of 'tie' constraints (see Section 4.4). If this is true, then one should generally not divert from the advice of Stryker regarding screw configuration, unless there is a burning need for reducing stresses within the system, to offset those introduce by a larger nail for example.

5.3 DEGREE OF WEIGHT-BEARING

A novel investigation into the effect that the amount of weight beared can have on healing was also conducted since, it would grant surgeons with an informed recommendation as to how swiftly patients should begin to bear their weight post-surgery. Moreover, it could help to inform their treatment strategy for a range of more unique body types from the skinny to morbidly obese.

Here, 0, 25%, 50% and 75% BW were arbitrarily chosen the for the analyses. In each case, the joint contact forces within the base model were scaled by the necessary amount and the muscle forces were retained, given that individuals preserve their leg swinging action to some extent even when bearing no weight.

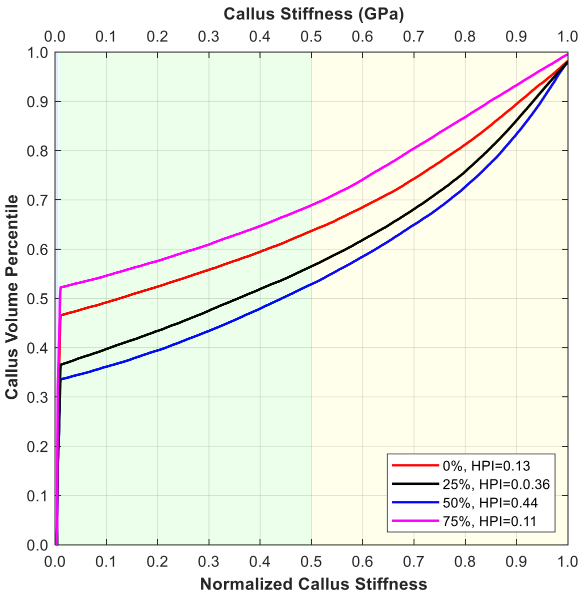

FIGURE 54 | Healing performance plot for different degrees of weight bearing.

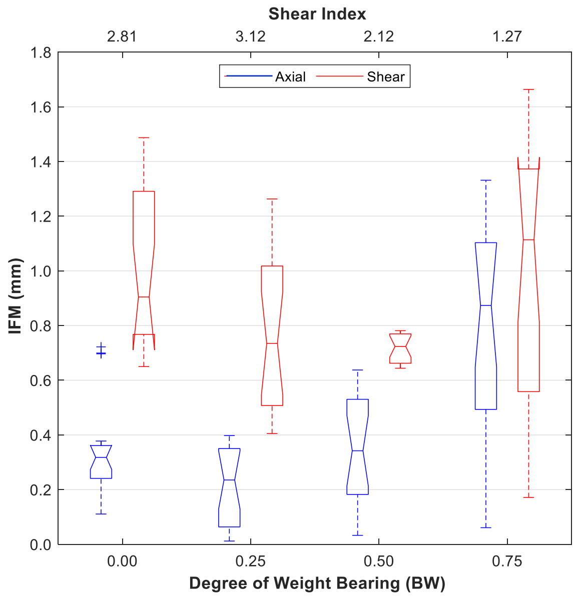

FIGURE 55 | Axial and shear IFMs for different degrees of weight bearing.

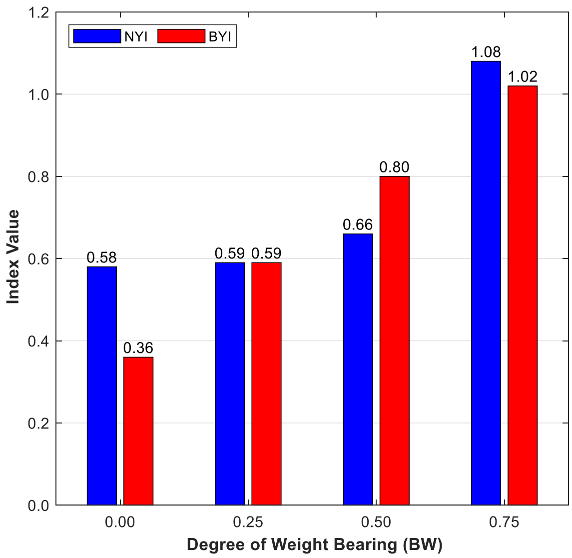

FIGURE 56 | NYIs and BYIs for different degrees of weightbearing.

The results derived for this study are fascinating, since they go completely against ones intuition. Under no weight bearing, there are no joint loads to help balance out the muscle loads, giving rise to some considerable degree of instability, yet under excessive loads the muscles have a negligible dampening effect, again promoting great instabilities. Consequently, must be some optimal weight bearing percentage that lies roughly central to these two extremes. Figure 54 suggest that this is 50%. Such a finding is a significant one since many individuals choose not to bear weight, with the logic that that the fracture will heal faster, yet in actual fact they are doing the opposite to what they truly desire!

5.4 REVISIONARY SURGICAL TECHNIQUES

If an LB fracture fails to heal in a reasonable time frame then one must typically undergo exchange nail surgery wherein the old osseointegrated nail in aggressively hammered out of the bone and replaced with a new, thicker one of much improved rigidity. Since this procedure is so invasive, this final study sought to establish whether 2 or 3 small, minimally invasive percutaneous screws placed perpendicular to the fracture plane could achieve the a similar result.

Non-union is always diagnosed in the final stages of healing when the system is so unstable that cartilaginous tissue is unable to differentiate into bone. Therefore, all calluses were first assigned the material properties of cartilage ($E = 50\ MPa,\ v = 0.167$). Exchange nails are also always chosen to be 1 or 2 mm larger in diameter than the nail they replace. Hence, a 10 mm non-union case, and an 11 and 12 mm exchange nail case were next composed. Finally, 1-2, 1-3, 2-3 and 1-2-3 configurations of percutaneous screws (see FIGURE 57) were all modelled in the hope that an optimal configuration could be identified.

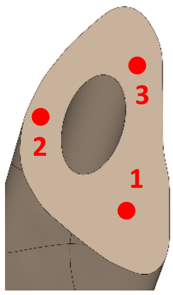

FIGURE 57 | Location of percutaneous screws.

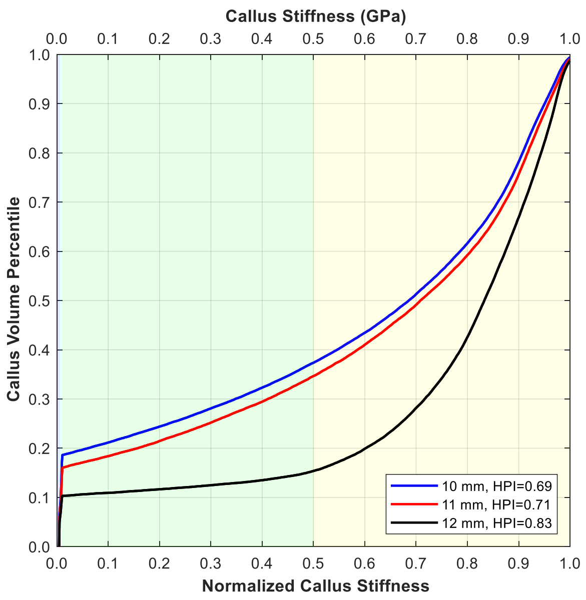

FIGURE 58 | Healing performance plot for a cartilaginous callus and different nail diameters.

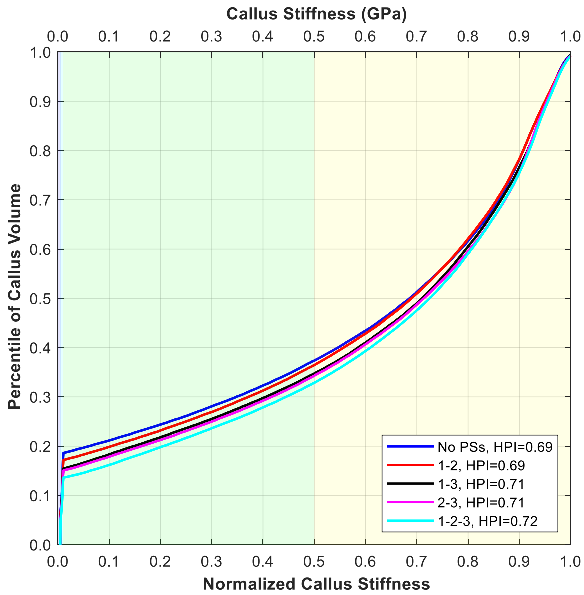

FIGURE 59 | Healing performance plot for a cartilaginous callus and different configurations of percutaneous screws.

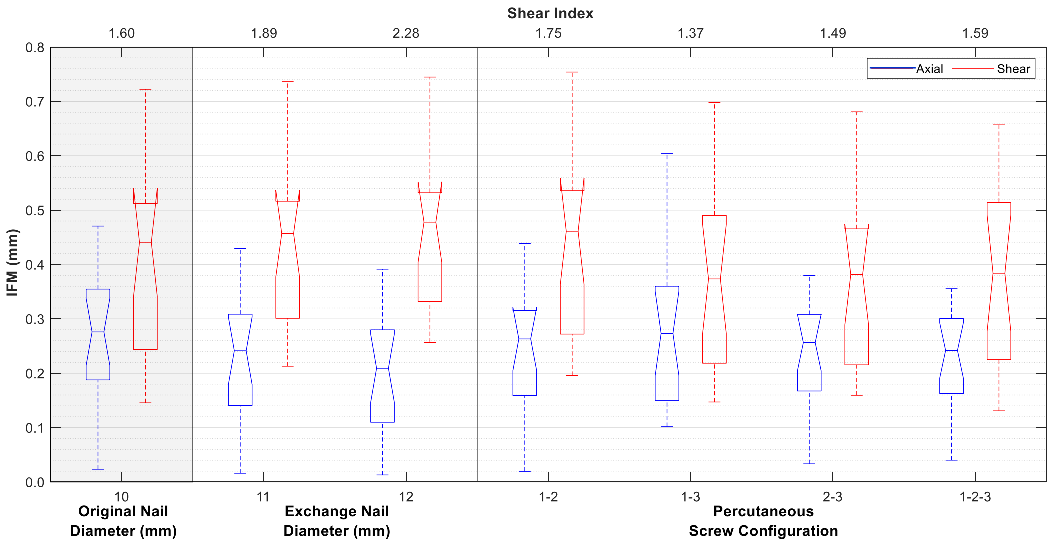

FIGURE 60 | Healing performance plot for a cartilaginous callus and different configurations of percutaneous screws.

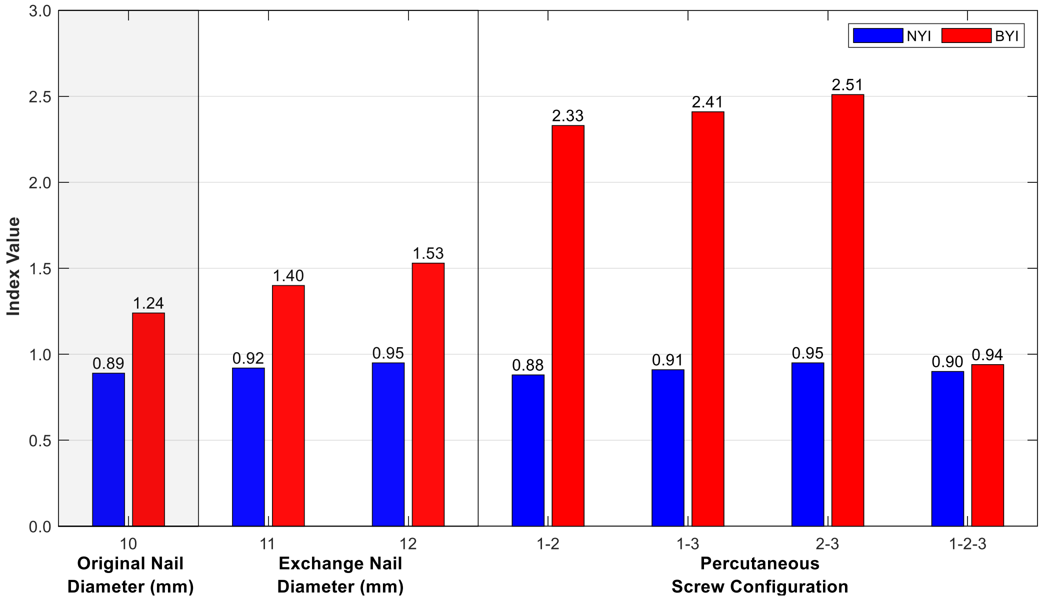

FIGURE 61 | NYIs and BYIs for different exchange nail diameters and different percutaneous screw configurations, as compared to the untreated case.

It can be seen from the FIGURES 58 and 59 that a 1-2-3 percutaneous screw configuration achieves virtually the same HPI as an 11 mm exchange nail, together with a much reduced set of system stresses (FIGURE 61). Hence, the former may be regarded a superior alternative to the latter from a mechanical perspective and there is much evidence to support its preferential adoption, clinically.

One can also infer that configuration 1-2 should never be implemented, as it only acts to raise the average stress in the system (FIGURE 21), without stabilizing the fracture. Moreover, configurations 1-3 and 2-3 perform almost identically from a mechanical perspective, delivering an HPI the same as the 11 mm exchange nail, yet transferring almost double the amount of stress to the surrounding bone. This suggests that percutaneous screws may be effective in an individual with an awkwardly shaped fracture site that permits just two screws to be fitted, although much diligence ought to be taken to ensure that the edge margin for the screws is sufficiently large that fracture will not occur in such cases.

6 LIMITATIONS & FUTURE WORK

Aside from the standard drawbacks that are brought with the adoption of the FE technique (of which there numerous, each having been touched upon elsewhere in this report), the present study has three main limitations and avenues for exploration in future research. The most significant of these is the notable absence of any experimental validation technique. A study that closely replicates the base model, ascertains the structure's compliance and compares this directly with the FE results would prove beneficial, potentially rocketing the integrity of all work presented. Furthermore, following the outcomes of the first parametric study, it would be reasonable to postulate that the size and shape of callus for a given fracture geometry could have marked effect on the findings acquired. Hence, the development of a shape prediction algorithm that can be run to prior to each of the main analyses would be valuable. A further step beyond this would then be to couple the code with an iterative analyses in which the properties of the callus are updated after each time step, allowing the full healing pathway to be investigated. Finally, the work presented here has focused solely on fractures of the tibia, yet LB fractures of the femur are almost as prevalent. Therefore, a study that replicates the one conducted here for femoral geometries, would clearly have its place amidst this field of work.

7 CONCLUSION

A systematic and meticulous approach to modelling has enabled an inexperienced, but resilient and determined FE analyst to devise an intricate, novel and tunable FE framework that allows the yielding of long-bone fracture constructs, as well as fracture site stability, and its healing potential to be quantitatively and simultaneously assessed with accuracy and precision, in a single analysis, for the first time. This is evidenced by the outcomes of innumerable sensitivity studies that were conducted to critically assess all assumptions and simplifications underpinning the model.

Fractures of greater obliquity, with larger gaps, and of orientation that tends towards the AP direction, have all been shown to have a deleterious effect on healing. In terms of the construct, larger nail diameters can rocket stability, yet the screw configuration appears to have little effect and should only be used as a means of a redistributing the stresses in a system. Moreover, 50% BW weightbearing ought to be advised to patients, with no and full weight bearing being strongly discouraged, if their chances of uneventful recovery are to be maximized. For cases of non-union, it has been shown that a set of three percutaneous screws perpendicular to the facture should always be considered as a serious alternative to exchange nailing, since they can offer a similar degree of added stability in a far less invasive manner.

This comprehensive package of fresh, unambiguous findings that can be comprehended, trusted and called upon by surgeons to inform the selection of an optimal construct configuration for each of their patients is hoped to help suppress the prevalence of non-unions in today's society.

7 REFERENCES

[1] **J. Chester**. Minimally Invasive Treatment of Long-Bone Fractures: A Finite Element Analysis Project Plan, 2020.

[2] **T. Jennison and M. Brinsden**. Fracture admission trends in England over a ten-year period.

[3] **M. Bottlang *et al.*** Biomechanical concepts for fracture fixation. *Journal of Orthopaedic Trauma*. vol. 29, no. 0 12. pp. S28–S33. 2015.

[4] **S. M. Tucker, H. Wee, E. Fox, J. S. Reid, and G. S. Lewis**. Parametric Finite Element Analysis of Intramedullary Nail Fixation of Proximal Femur Fractures. *Journal of Orthopaedic Research*. vol. 37, no. 11. pp. 2358–2366. 2019.

[5] **A. Trompeter**. A call to arms: it's time to bear weight! *The Bone & Joint Journal*. vol. 102, no. 4. pp. 403–406. 2020.

[6] **B. L. Norris, G. Lang, T. A. T. Russell, D. L. Rothberg, W. M. Ricci, and J. Borrelli**. Absolute Versus Relative Fracture Fixation: Impact on Fracture Healing. *Journal of Orthopaedic Trauma*. vol. 32. pp. S12–S16. 2018.

[7] **S. K. Stewart**.Fracture non-union: A review of clinical challenges and future research needs, *Malaysian Orthopaedic Journal*, vol. 13, no. 2. Malaysian Orthopaedic Association, pp. 1–10, Jul. 01, 2019.

[8] **A. O. Usoro, A. Bhashyam, A. Mohamadi, G. S. Dyer, L. Zirkle, and A. Von Keudell**.Clinical Outcomes and Complications of the Surgical Implant Generation Network (SIGN) Intramedullary Nail: A Systematic Review and Meta-Analysis, *Journal of Orthopaedic Trauma*, vol. 33, no. 1. Lippincott Williams and Wilkins, pp. 42–48, Jan. 01, 2019.

[9] **M. E. Cain, L. A. M. Hendrickx, N. J. Bleeker, K. T. A. Lambers, J. N. Doornberg, and R. L. Jaarsma**. Prevalence of Rotational Malalignment After Intramedullary Nailing of Tibial Shaft Fractures: Can We Reliably Use the Contralateral Uninjured Side as the Reference Standard? *The Journal of bone and joint surgery. American volume*. vol. 102, no. 7. pp. 582–591. 2020.

[10] **L. A. Mills, S. A. Aitken, A. Hamish, and R. W. Simpson.** The risk of non-union per fracture: current myths and revised fi gures from a population of over 4 million adults. *Acta Orthopaedica*. vol. 88, no. 4. pp. 434–439. 2017.

[11] **N. K. Kanakaris and P. V. Giannoudis.** The health economics of the treatment of long-bone non-unions. *Injury*. vol. 38, no. SUPPL. 2. pp. S77–S84. 2007.

[12] Fracture and Dislocation Compendium-2018. 2018.

[13] **G. Marongiu, A. Dolci, M. Verona, and A. Capone**.The biology and treatment of acute long-bones diaphyseal fractures: Overview of the current options for bone healing enhancement, *Bone Reports*, vol. 12. Elsevier Inc, Jun. 01, 2020.

[14] **N. Ali *et al.*** Treatment of extra-articular distal tibial fractures: Minimally invasive percutaneous plate osteosynthesis versus intramedullary nailing. *Trauma Monthly*. vol. 22, no. 4. 2017.

[15] **H. Schmal *et al.*** Nonunion - consensus from the 4th annual meeting of the danish orthopaedic trauma society. *EFORT Open Reviews*. vol. 5, no. 1. pp. 46–57. 2020.

[16] **D. S. Elliott *et al.*** A unified theory of bone healing and nonunion. *Bone and Joint Journal*. vol. 98B, no. 7. pp. 884–891. 2016.

[17] **S. M. Perren**. The biomechanics and biology of internal fixation using plates and nails. *Orthopedics*. vol. 12, no. 1. pp. 21–34. 1989.

[18] **R. Wenger, F. Oehme, J. Winkler, S. M. Perren, R. Babst, and F. J. P. Beeres**. Absolute or relative stability in minimal invasive plate osteosynthesis of simple distal meta or diaphyseal tibia fractures? *Injury*. vol. 48, no. 6. pp. 1217–1223. 2017.

[19] **T. N. Gardner, T. Stoll, L. Marks, S. Mishra, and M. Knothe Tate.** The influence of mechanical stimulus on the pattern of tissue differentiation in a long bone fracture - an FEM study, 2000.

[20] **R. Zura *et al.*** Epidemiology of fracture nonunion in 18 human bones. *JAMA Surgery*. vol. 151, no. 11. 2016.

[21] **R. G. Pearson, R. G. E. Clement, and L. Edwards**. Do smokers have greater risk of delayed and non-union after fracture, osteotomy and arthrodesis? A systematic review with meta-analysis.

[22] **R. Jenkinson and H. J. Kreder**. Principles of Internal Fixation of Fractures. in *Encyclopedia of Trauma Care*, Springer Berlin Heidelberg. 2015. pp. 1321–1340.

[23] **A. Kothari, P. Monk, and R. Handley**. Percutaneous Strain Reduction Screws-A Safe and Simple Surgical Option for Problems With Bony Union. A Technical Trick. *Journal of orthopaedic trauma*. vol. 33, no. 4. pp. e151–e157. 2019.

[24] **A. Mehboob, H. Mehboob, S. H. Chang, and F. Tarlochan**. Effect of composite intramedullary nails (IM) on healing of long bone fractures by means of reamed and unreamed methods. *Composite Structures*. vol. 167. pp. 76–87. 2017.

[25] **A. Mehboob and S. H. Chang**. Effect of composite bone plates on callus generation and healing of fractured tibia with different screw configurations. *Composites Science and Technology*. vol. 167. pp. 96–105. 2018.

[26] **S. Pitjamit, W. Nakkiew, K. Thongkorn, W. Thanakulwattana, and K. Thunsiri**. Finite element analysis of traditional and new fixation techniques of the 3d-printed composite interlocking nail in canine femoral shaft fractures. *Applied Sciences (Switzerland)*. vol. 10, no. 10. 2020.

[27] **J. Lu, S. C. Guo, Q. Y. Wang, J. G. Sheng, and S. C. Tao**. J-bone graft with double locking plate: A symphony of mechanics and biology for atrophic distal femoral non-union with bone defect. *Journal of Orthopaedic Surgery and Research*. vol. 15, no. 1. 2020.

[28] **D. Takahashi *et al.*** Finite element analysis of double-plate fixation using reversed locking compression-distal femoral plates for Vancouver B1 periprosthetic femoral fractures. 2020.

[29] **C.-K. Chao, Y.-L. Chen, J. Lin, and J. Lin**. BJR Half-threaded holes markedly increase the fatigue life of locking plates without compromising screw stability aims. vol. 9, no. 10. 2020.

[30] **Y. Cao, Y. Zhang, L. Huang, and X. Huang**. The impact of plate length, fibula integrity and plate placement on tibial shaft fixation stability: A finite element study. *Journal of Orthopaedic Surgery and Research*. vol. 14, no. 1. 2019.

[31] **W. Sheng, A. Ji, R. Fang, G. He, and C. Chen**. Finite Element-and Design of Experiment-Derived Optimization of Screw Configurations and a Locking Plate for Internal Fixation System. *Computational and Mathematical Methods in Medicine*. vol. 2019. 2019.

[32] **F. Chen *et al.*** Finite element analysis of intramedullary nailing and double locking plate for treating extra-articular proximal tibial fractures. *Journal of Orthopaedic Surgery and Research*. vol. 13, no. 1. 2018.

[33] **C. Jacquet *et al.*** Adding a protective screw improves hinge's axial and torsional stability in High Tibial Osteotomy. *Clinical Biomechanics*. vol. 74. pp. 96–102. 2020.

[34] **D. Kluess**. Finite element analysis in orthopaedic biomechanics. *Finite element analysis*. no. August 2010. pp. 151–171. 2010.

[35] **X. J. Hu and H. Wang**. Biomechanical assessment and 3D finite element analysisof the treatment of tibial fractures using minimallyinvasive percutaneous plates. *Experimental and Therapeutic Medicine*. vol. 14, no. 2. pp. 1692–1698. 2017.

[36] **S. Gabarre, J. Albareda, L. Gracia, S. Puértolas, E. Ibarz, and A. Herrera**. Influence of gap size, screw configuration, and nail materials in the stability of anterograde reamed intramedullary nail in femoral transverse fractures. *Injury*. vol. 48. pp. S40–S46. 2017.

[37] **A. Mehboob, S. H. A. Rizvi, S. H. Chang, and H. Mehboob**. Comparative study of healing fractured tibia assembled with various composite bone plates. *Composites Science and Technology*. vol. 197. 2020.

[38] **P. Schwarzenberg, K. Klein, S. J. Ferguson, B. von Rechenberg, S. Darwiche, and H. L. Dailey**. Virtual mechanical tests out-perform morphometric measures for assessment of mechanical stability of fracture healing in vivo. *Journal of Orthopaedic Research*. 2020.

[39] **A. Mehboob and S. H. Chang**. Effect of initial micro-movement of a fracture gap fastened by composite prosthesis on bone healing. *Composite Structures*. vol. 226. 2019.

[40] **S. Ghimire, S. Miramini, M. Richardson, P. Mendis, and L. Zhang**. Effects of dynamic loading on fracture healing under different locking compression plate configurations: A finite element study. *Journal of the Mechanical Behavior of Biomedical Materials*. vol. 94. pp. 74–85. 2019.

[41] **A. Mehboob and S. H. Chang**. Biomechanical simulation of healing process of fractured femoral shaft applied by composite intramedullary nails according to fracture configuration. *Composite Structures*. vol. 185. pp. 81–93. 2018.

[42] **A. Mehboob, H. Mehboob, J. Kim, S. H. Chang, and F. Tarlochan**. Influence of initial biomechanical environment provided by fibrous composite intramedullary nails on bone fracture healing. *Composite Structures*. vol. 175. pp. 123–134. 2017.

[43] **G. N. Duda *et al.*** Mechanical boundary conditions of fracture healing: borderline indications in the treatment of unreamed tibial nailing, 2001.

[44] **G. N. Duda, M. Heller, J. Albinger, O. Schulz, E. Schneider, and L. Claes**. Influence of muscle forces on femoral strain distribution. *Journal of Biomechanics*. vol. 31, no. 9. pp. 841–846. 1998.

[45] **E. J. Strauss, D. Alfonso, F. J. Kummer, K. A. Egol, and N. C. Tejwani**. The effect of concurrent fibular fracture on the fixation of distal tibia fractures: A laboratory comparison of intramedullary nails with locked plates. *Journal of Orthopaedic Trauma*. vol. 21, no. 3. pp. 172–177. 2007.

[46] **F. W. Hoegel, S. Hoffmann, P. Weninger, V. Bühren, and P. Augat**. Biomechanical comparison of locked plate osteosynthesis, reamed and unreamed nailing in conventional interlocking technique, and unreamed angle stable nailing in distal tibia fractures. *Journal of Trauma and Acute Care Surgery*. vol. 73, no. 4. pp. 933–938. 2012.

[47] **N. Rosa *et al.*** Recent developments on intramedullary nailing: A biomechanical perspective. *Annals of the New York*

Academy of Sciences. vol. 1408. 2017.

[48] **M. L. Costa *et al.*** Intramedullary nail fixation versus locking plate fixation for adults with a fracture of the distal tibia: The UK fixDT RCT. *Health Technology Assessment*. vol. 22, no. 25. pp. 1–147. 2018.

[49] **M. A. Bagheri and G. Rouhi**. Design and numerical investigation of an adaptive intramedullary nail with a novel interlocking mechanism. *Journal of Computational Design and Engineering*. vol. 7, no. 6. pp. 722–735. 2020.

[50] **G. N. Duda *et al.*** Mechanical boundary conditions of fracture healing: borderline indications in the treatment of unreamed tibial nailing, 2001.

[51] **V. Buhren, K. Dickson, and P. Tornetta**. T2 Tibial Nailing System, 2019.

[52] **M. White**. Intramedullary Nailing, 2018.

[53] **M. Bhandari *et al.*** Randomized trial of reamed and unreamed intramedullary nailing of tibial shaft fractures. *Journal of Bone and Joint Surgery - Series A*. vol. 90, no. 12. pp. 2567–2578. 2008.

[54] **E. Ocalan, C. Cagri Ustun, and K. Aktuglu**. Reamed vs. Unreamed Intramedullary Nailing of Femoral Fractures in the Elderly, 2017. Accessed: Feb. 04, 2021. [Online]. Available: http://www.imedpub.com/.

[55] **A. B. Li, W. J. Zhang, W. J. Guo, X. H. Wang, H. M. Jin, and Y. M. Zhao**.Reamed versus unreamed intramedullary nailing for the treatment of femoral fractures A meta-analysis of prospective randomized controlled trials, *Medicine (United States)*, vol. 95, no. 29. Lippincott Williams and Wilkins, Jul. 26, 2016.

[56] **R. Krone and P. Schuster**. An Investigation on the Importance of Material Anisotropy in Finite-Element Modeling of the Human Femur, 2006.

[57] ANSYS Contact Technology Guide, 2018.

[58] **H. J. Kim, S. H. Kim, and S. H. Chang**. Bio-mechanical analysis of a fractured tibia with composite bone plates according to the diaphyseal oblique fracture angle. *Composites Part B: Engineering*. vol. 42, no. 4. pp. 666–674. 2011.

[59] **M. F. Hoffmann, C. B. Jones, D. L. Sietsema, P. Tornetta, and S. J. Koenig**. Clinical outcomes of locked plating of distal femoral fractures in a retrospective cohort. *Journal of Orthopaedic Surgery and Research*. vol. 8, no. 1. pp. 1–9. 2013.

[60] **A. MacLeod, A. H. R. W. Simpson, and P. Pankaj**. Experimental and numerical investigation into the influence of loading conditions in biomechanical testing of locking plate fracture fixation devices. *Bone & Joint Research*. vol. 7, no. 1. pp. 111–120. 2018.

[61] **M. Moazen, J. H. Mak, A. C. Jones, Z. Jin, R. K. Wilcox, and E. Tsiridis**. Evaluation of a new approach for modelling the screw-bone interface in a locking plate fixation: A corroboration study. *Proceedings of the Institution of Mechanical Engineers, Part H: Journal of Engineering in Medicine*. vol. 227, no. 7. pp. 746–756. 2013.

[62] **A. R. MacLeod, G. Serrancoli, B. J. Fregly, A. D. Toms, and H. S. Gill**. The effect of plate design, bridging span, and fracture healing on the performance of high tibial osteotomy plates an experimental and finite element study. *Bone and Joint Research*. vol. 7, no. 12. pp. 639–649. 2018.

[63] **Z. Ming, D. Xiang, and F. Yubo**.Stress analysis of osseointegrated transfemoral prosthesis: A finite element model, in *Annual International Conference of the IEEE Engineering in Medicine and Biology - Proceedings*, 2005, vol. 7 VOLS, pp. 4060–4063.

[64] **D. Croccolo, M. De Agostinis, S. Fini, S. Funaioli, G. Olmi, and F. Robusto**. Experimentally validated structural finite element method analysis of a tibial intramedullary nail: Optimal choice of the contact settings. *Proceedings of the Institution of Mechanical Engineers, Part H: Journal of Engineering in Medicine*. vol. 233, no. 2. pp. 193–206. 2019.

[65] **R. A. Toupin**. On St. Venant's principle. in *Applied Mechanics*, Springer Berlin Heidelberg. 1966. pp. 151–152.

[66] **T. Wehner, L. Claes, and U. Simon**. Internal loads in the human tibia during gait. *Clinical Biomechanics*. vol. 24, no. 3. pp. 299–302. 2009.

[67] **E. Schneider, M. C. Michel, M. Genge, K. Zuber, R. Ganz, and S. M. Perren**.Loads acting in an intramedullary nail during fracture healing in the human femur, in *Journal of Biomechanics*, 2001, vol. 34, no. 7, pp. 849–857.

[68] **A. Mehboob, H. Mehboob, S. H. Chang, and F. Tarlochan**. Effect of composite intramedullary nails (IM) on healing of long bone fractures by means of reamed and unreamed methods. *Composite Structures*. vol. 167. pp. 76–87. 2017.

[69] **J. B. Fixlay, R. B. Bournet, and J. Mclean**. A TECHNIQUE FOR THE IN VITRO MEASUREMENT OF PRINCIPAL STRAINS IN THE HUMAN TIBIA*.

[70] **L. E. Lanyon, W. G. J. Hampson, A. E. Goodship, and J. S. Shah**. Bone deformation recorded in vivo from strain gauges attached to the human tibial shaft. *Acta Orthopaedica*. vol. 46, no. 2. pp. 256–268. 1975.

[71] **K. J. Goodwin and N. A. Sharkey**. Material properties of interstitial lamellae reflect local strain environments, 2002. [Online]. Available: www.elsevier.coni/locate/ortlires.

[72] **N. B. Damm, M. M. Morlock, and N. E. Bishop**. Friction coefficient and effective interference at the implant-bone interface. *Journal of Biomechanics*. vol. 48, no. 12. pp. 3517–3521. 2015.

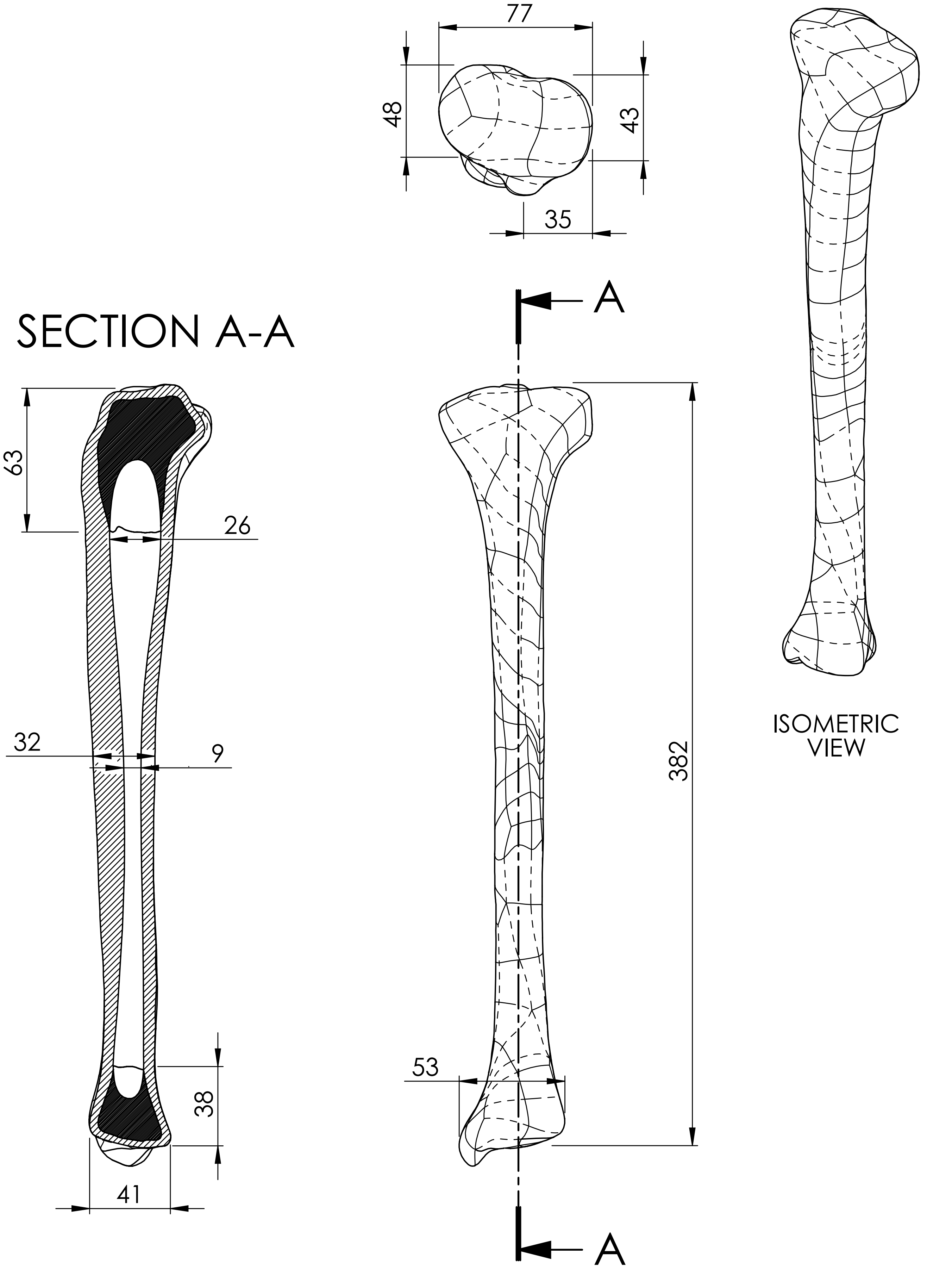

TOLERANCES
X = ± 0.5
X.X = ± 0.1
X.XX = ± 0.02
ANGULAR ±1°
SURFACE FINISH MACHINED FACES Ra 6.3

THIRD ANGLE PROJECTION

MATERIAL:
HUMAN CORTICAL AND TRABECULAR BONE

ALL DIMENSIONS ARE IN MILLIMETRES

	NAME	DATE
DRAWN	J. CHESTER	26/05/21
CHECKED		
APPROVED		

DO NOT SCALE DRAWING

A4 SCALE 3:8

TITLE:
MODIFIED SAWBONES 3401 TIBIA

DWG No.
SKU3401

Imperial College London
Department of Mechanical Engineering

SHEET 1 OF 1 REVISION 1

- ⌀5 CENTRAL CAVITY THROUGH ALL
- ALL HOLES ⌀5 AND CHAMFERED 1 X 45°
- ALL EDGES FILLETED R1, UNLESS STATED OTHERWISE

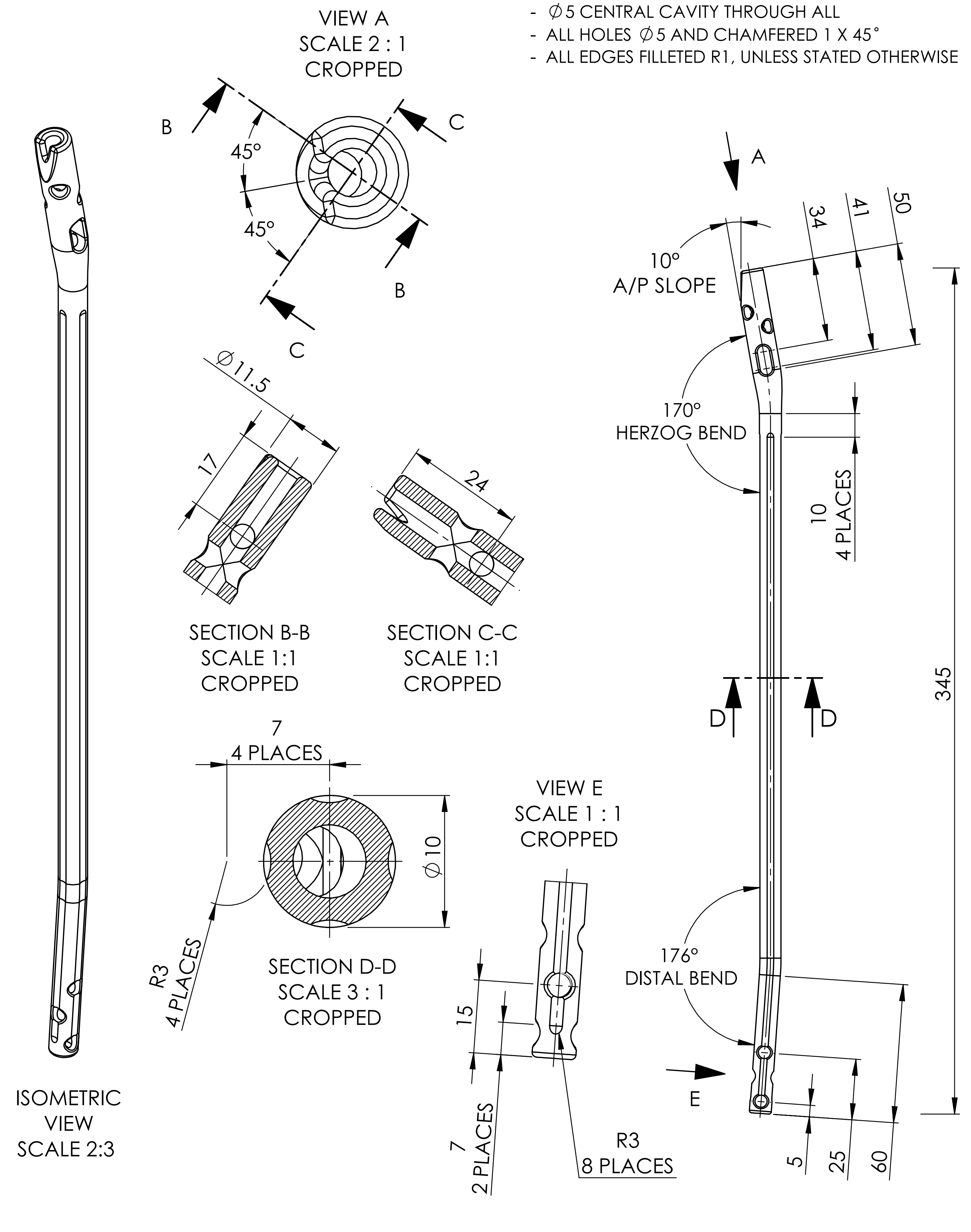

TOLERANCES		THIRD ANGLE PROJECTION	MATERIAL: TI6AL4V	TITLE: STRYKER T2 STANDARD TIBIAL NAIL 10 X 345
X = ± 0.5 X.X = ± 0.1 X.XX = ± 0.02	ANGULAR ±1° SURFACE FINISH MACHINED FACES Ra 6.3		ALL DIMENSIONS ARE IN MILLIMETRES	
	NAME	DATE		
DRAWN	J. CHESTER	11/12/20	DO NOT SCALE DRAWING	DWG No. 1822-1034S
CHECKED			A4	SCALE 1:2
APPROVED				

Imperial College London
Department of Mechanical Engineering

SHEET 1 OF 1 | REVISION 1